Silurian-Devonian Lithospheric Thinning and Thermally Softening Along the Northern Margin of the Tarim Craton: Geological Mapping, Petro-Structural Analysis and Geochronological Constraints

Jun Ning, Ying-de Jiang, Karel Schulmann, Sheng Wang, Peng-fei Li, Shuai Shi, Hua-ning Qiu

Tectonics®

RESEARCH ARTICLE
10.1029/2023TC007792

Key Points:

- NE Tarim Craton formed a sub-horizontal HT/LP foliation in response to crustal extension in the late Silurian-early Devonian
- Thinned and thermally softened northern Tarim margin was affected by middle Devonian shortening
- Early Paleozoic northern Tarim, South Tianshan, and Central Tianshan evolved into one supra-subduction environment

Supporting Information:

Supporting Information may be found in the online version of this article.

Correspondence to:

Y.-D. Jiang,
jiangyd@gig.ac.cn

Citation:

Ning, J., Jiang, Y.-D., Schulmann, K., Wang, S., Li, P.-F., Shi, S., & Qiu, H.-N. (2023). Silurian-Devonian lithospheric thinning and thermally softening along the northern margin of the Tarim Craton: Geological mapping, petro-structural analysis and geochronological constraints. *Tectonics*, *42*, e2023TC007792. https://doi.org/10.1029/2023TC007792

Received 7 FEB 2023
Accepted 13 AUG 2023
Corrected 9 OCT 2023

This article was corrected on 9 OCT 2023. See the end of the full text for details.

Silurian-Devonian Lithospheric Thinning and Thermally Softening Along the Northern Margin of the Tarim Craton: Geological Mapping, Petro-Structural Analysis and Geochronological Constraints

Jun Ning[1,2,3], Ying-De Jiang[1,2], Karel Schulmann[4,5], Sheng Wang[6], Peng-Fei Li[1,2], Shuai Shi[1,2,3], and Hua-Ning Qiu[7]

[1]State Key Laboratory of Isotope Geochemistry, Guangzhou Institute of Geochemistry, Chinese Academy of Sciences, Guangzhou, China, [2]CAS Center for Excellence in Deep Earth Science, Guangzhou, China, [3]University of Chinese Academy of Sciences, Beijing, China, [4]Centre for Lithospheric Research, Czech Geological Survey, Prague, Czech Republic, [5]Université de Strasbourg, CNRS, ITES, Strasbourg, France, [6]School of Civil Engineering, Anhui Jianzhu University, Hefei, China, [7]Key Laboratory of Tectonics and Petroleum Resources, Ministry of Education, China University of Geoscience, Wuhan, China

Abstract While the western part of northern Tarim Craton has long been considered as a Paleozoic passive margin, a pronounced Silurian-Devonian magmatism developed on eastern part of this margin may indicate different but active margin setting. In this contribution, detailed structural mapping, petro-structural analysis, and geochronological investigations were conducted in the Korla area, eastern part of northern Tarim Craton. Three main generations of fabrics were recognized. The earliest pervasive fabric is an originally sub-horizontal metamorphic S1 foliation that is in part associated with migmatization characterized by high temperature/low pressure metamorphic mineral assemblages, interpreted as reflecting crustal extension. S1 foliation was affected by D2 contraction forming regional-scale F2 upright folds associated with sub-vertical axial planar foliation S2. D3 is marked by development of NW-SE oriented dextral fault, asymmetric mega-folding of S2 and spaced NW-SE-striking S3 foliation, likely in response to dextral transpression. Geochronological data indicate that D1 extension occurred from ca. 420 to 410 Ma, D2 contraction started around 410 Ma and lasted till 400 Ma or later, and D3 transpression was ongoing around ~370 Ma. Integrated with regional data, an updated geodynamic model is proposed by interpreting the Central Tianshan, South Tianshan and NE Tarim Craton as an early Paleozoic supra-subduction system. We suggest that the Silurian-Devonian event reflects thermal softening and horizontal stretching of the supra-subduction crust, resulting in drifting of the Central Tianshan continental arc from the proto Tarim Craton in association with opening of the South Tianshan back-arc basin in-between.

1. Introduction

During the Paleozoic, continental blocks including the North China and Tarim cratons and other smaller blocks, such as the Dunhuang block, drifted northward from the northern margin of the Gondwana continent across the Paleo-Asian Ocean toward the Laurasian and Siberian landmasses to the north (Merdith et al., 2021; Metcalfe, 2013; Stampfli & Borel, 2002; Zhao et al., 2018). The timing of separation of these continental blocks from Gondwana occurred in the late Neoproterozoic to early Paleozoic (Xu et al., 2011; Zhao et al., 2018), while their Silurian to Devonian mutual amalgamation resulted in formation of a ribbon-like continental assemblage (Domeier, 2018; Merdith et al., 2021). Meanwhile, a giant accretionary system known as the Central Asian Orogenic Belt (CAOB) or Altaids (Glen, 2013; Rod, 2007; Sengör et al., 1993; Wilhem et al., 2012; Xiao et al., 2020) formed at the periphery of the exterior Paleo-Pacific Ocean. The collision of the northward moving Tarim-North China continental ribbon system (also known as the North China-Tarim collage of Xiao et al. (2015)) with the southern part of the CAOB during the Carboniferous to Permian hallmarks the final closure of the Paleo-Asian Ocean and end of oceanic accretion of the CAOB system. In this conceptual model, the Paleo-Asian Ocean was consumed via north-dipping subduction (Pei et al., 2016; Z. W. Wang et al., 2016b; Xiao et al., 2008, 2009a; S. H. Zhang et al., 2014). However, this model is challenged by extensive early Paleozoic magmatism along the northern margins of both Tarim and North China cratons, which have been interpreted as typical Andean-type active margins at the time (Ge et al., 2012a; Lin et al., 2013; Q. G. Mao et al., 2012; Qin et al., 2016; Soldner, Yuan,

et al., 2022; Xu, Charvet, et al., 2013; T. Zhu et al., 2019a). It remains unclear whether this magmatic activity reflected closure of relatively small oceanic domains between Tarim and North China cratons and their peripheral continental domains (Cui et al., 2018; Fu et al., 2018; H. Yang et al., 2015) or the arc-related magmatism induced by southward subduction of the large Paleo-Asian Ocean (Ge et al., 2012a; Xiao, Windley, Yong, et al., 2009).

The Paleozoic tectonic evolution of the northern Tarim Craton is exactly in the core of this discussion. The Tarim Craton has long been considered as a continental block that rifted away from the northern Gondwana continent during the early Paleozoic and drifted northward till the late Paleozoic when it collided with the Kazakhstan collage of the CAOB (Jahn, 2004; S. Z. Li et al., 2018; Metcalfe, 1994, 1996, 2013; Zhao et al., 2018). This concept is supported by development of early Paleozoic passive margin shallow marine deposits on the northwestern margin of the Tarim Craton, in particular in the Keping area (Allen et al., 1993; Windley et al., 1990; Xiao et al., 2005, 2008). Furthermore, a Devonian-Carboniferous accretionary complex containing eclogites in the northerly South Tianshan belt developed coevally with extensive arc magmatism further north along the southern margin of the Yili block of the Kazakhstan collage (Cao et al., 2017; Chen et al., 2012; Dong et al., 2011; J. Gao et al., 1995, 1998, 2000; Hu et al., 2007; J. S. Liu et al., 2022; S. H. Yang & Zhou, 2009; Zhong et al., 2017). The spatial distribution of passive margin, accretionary wedge and magmatic arc from south to north is compatible with a northward subduction of an oceanic domain terminated by amalgamation of the Tarim Craton with the CAOB. However, such a tectonic configuration is in contradiction with extensive Silurian-Devonian magmatism developed along the eastern segment of northern Tarim Craton, particularly in the Huola Mountain and Kuruktag area (R. Gao et al., 2012; Ge et al., 2012a; Guo et al., 2013; Kong et al., 2019; Lin et al., 2013; Qin et al., 2016; Z. X. Zhu et al., 2008). There, Silurian-Devonian magmatic rocks show relative enrichment in large ion lithophile elements (LILE), depletion in high field strength elements (HFSE) and variable zircon Hf isotopic compositions, leading many authors to consider them to be typical arc-related rocks (Ge et al., 2012a, 2014b; Guo et al., 2013; Lin et al., 2013). Accordingly, the northern Tarim Craton, or at least its eastern part, was interpreted as a Silurian-Devonian Paleozoic active margin (Ge et al., 2012a; Guo et al., 2013; Huang et al., 2013a; Lin et al., 2013; Qin et al., 2016; M. Wang et al., 2016a; Zhong et al., 2019).

It is therefore apparent that the Paleozoic evolution of the eastern segment of northern Tarim is distinct from the western one. Moreover, while the Silurian-Devonian magmatism at the eastern part of northern Tarim margin has been widely documented, the metamorphic and structural evolution associated with this magmatism has been so far rarely investigated. To fill the gap, detailed geological and structural mapping accompanied with petro-structural observation, and zircon, monazite U-Pb and biotite $^{40}Ar/^{39}Ar$ geochronological studies were carried out in the Korla area, NE Tarim, a key region where the Silurian-Devonian magmatism has been widely documented. The data allow characterizing the structural and metamorphic evolution of NE Tarim and deciphering the geodynamic evolution of the region during the Silurian-Devonian.

2. Regional Geological Background

The eyeball-like shaped Tarim Craton, located at the southern border of the CAOB (Figure 1a), represents one of the oldest cratons in China. It is bounded by the Tianshan Mts. to the north and the Kunlun Mts. to the south. While the Taklimakan Desert occupies most of the central part of the Tarim Craton, the Precambrian basement rocks are mainly exposed along its northern, eastern and southwestern margins. Eoarchean tonalitic gneisses (ca. 3.70 Ga) identified in the Altyn Tagh area are considered to be the oldest basement rocks of the craton (Ge et al., 2018, 2020). Besides, a few occurrences of Mesoarchean tonalite-trondhjemite-granodiorite rocks (TTG) and amphibolite bodies have been recognized (Ge et al., 2022). Except these lithological units, the Precambrian basement is mainly composed of 2.80–2.57 Ga Neoarchean TTG and early Paleoproterozoic gneisses and marble (Ge et al., 2014a; X. P. Long et al., 2010b, 2011b; Shu et al., 2011; C. L. Zhang et al., 2013). These rocks were further affected by a 1.9–1.8 Ga metamorphic event (Ge et al., 2013, 2014a; Lei et al., 2012; X. P. Long et al., 2010b, 2011b; Shu et al., 2011; C. L. Zhang et al., 2012a) and were unconformably overlain by Mesoproterozoic low-grade metasedimentary rocks (C. L. Zhang et al., 2013). The latter sequences were intruded by Neoproterozoic plutons documented in Kuruktag area which were considered either as formed during break-up of the Rodinia supercontinent at around 800-650 Ma (C. Zhang et al., 2007; C. L. Zhang et al., 2013; W. B. Zhu et al., 2008) or as a product of arc magmatism (Ge et al., 2014b). Neoproterozoic blueschist-bearing rocks in northwestern Tarim Craton were interpreted as the manifestation of subsequent Gondwana assembly (Liou et al., 1989; W. B. Zhu et al., 2011). There, the Precambrian basement rocks are overlain by complete sequence

10.1029/2023TC007792

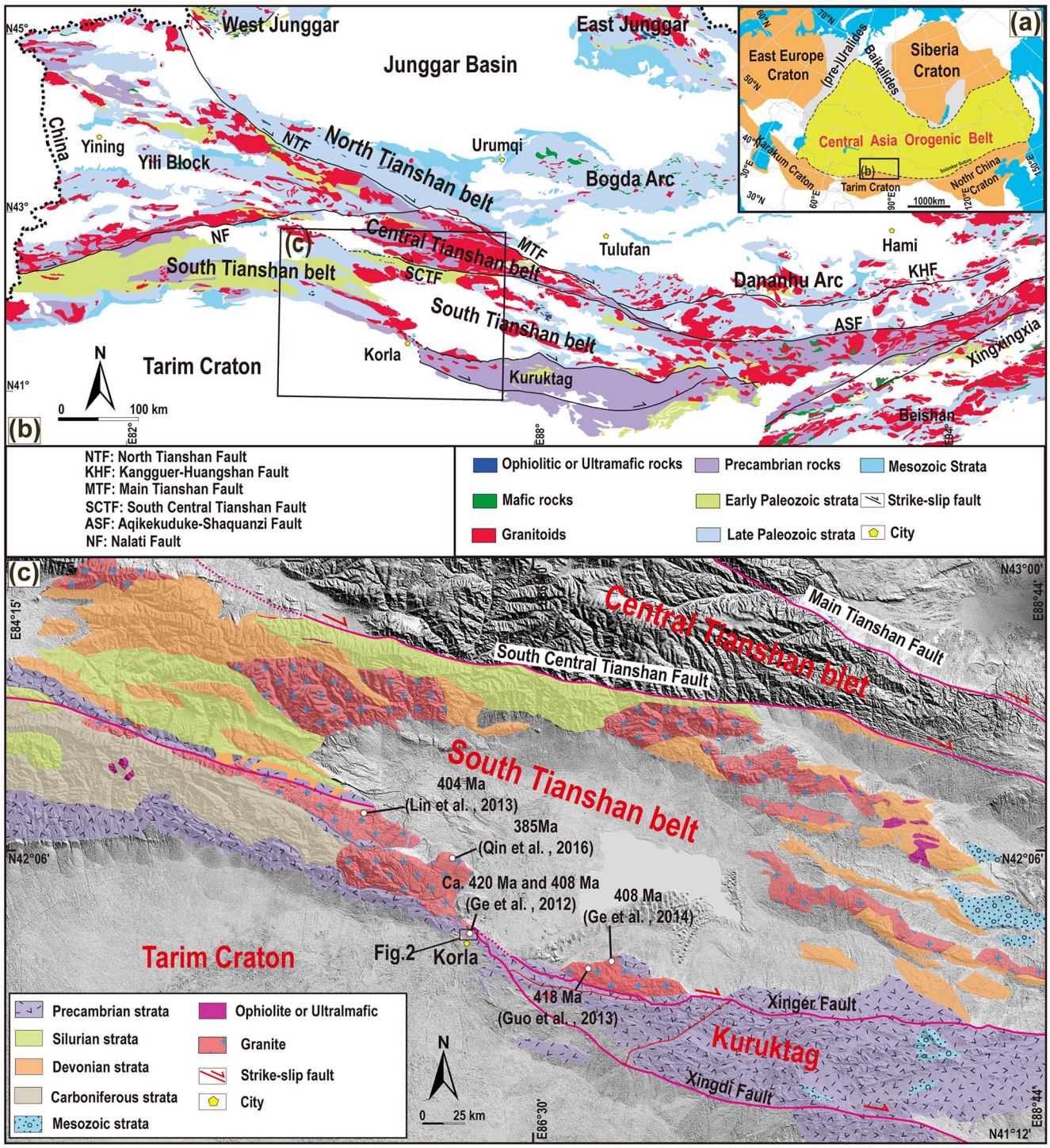

Figure 1. (a) Tectonic framework of the Central Asian Orogenic Belt and the surrounding cratons (modified after Sengör et al. (1993) and Xiao et al. (2013)). (b) Simplified geological map of the Chinese Tianshan Mts (modified after Li et al. (2020)). (c) Geological map of the eastern segment of northern Tarim and its adjacent area (modified after Li et al. (2020)). Available geochronological data of Silurian-Devonian magmatic rocks and their sources are: Ge et al. (2012a, 2014b), Guo et al. (2013), Lin et al. (2013), and Qin et al. (2016). The study area is also indicated by a rectangle.

of Cambrian to Carboniferous cherty limestone, chert and sandstone (Alexeiev et al., 2015; Lee, 1985). On the other hand, only shallow marine Devonian to Carboniferous sedimentary sequences are preserved in northeastern Tarim Craton (Allen et al., 1993; BGMRX, 1993). The sedimentary evolution of the craton is terminated by deposition of Permian terrigenous sediments interpreted to have formed in a continental extensional setting

(Carroll et al., 1995; Lee, 1985). Igneous rocks mainly occur along the northeastern margin of the Tarim Craton being represented by early Devonian gabbro and granitoid intrusions (Chen et al., 2019; Ge et al., 2012a; Guo et al., 2013; Lin et al., 2013) and early Permian A-type granites with their eruptive equivalents along the entire northern Tarim Craton and adjacent areas (Huang et al., 2014, 2018; L. L. Long et al., 2010a).

In the north, the Tarim Craton is in contact with the Chinese Tianshan Mts. that constitutes of several tectonic units and is generally considered as the southernmost extremity of the Kazakhstan collage of the CAOB (Sengör et al., 1993; Xiao et al., 2008). Geologically, the Chinese Tianshan Mts. is composed of island arcs, accretionary wedges and Precambrian blocks, with formation history ranging from late Proterozoic to late Paleozoic (Sengör et al., 1993; Windley et al., 2007). This mountain range is roughly divided into western and eastern segments by the NE-trending Nalati Fault (Figure 1b). The eastern segment comprises the North Tianshan belt, Central Tianshan belt and South Tianshan belt (Figure 1b), separated by two nearly W-E-striking parallel faults, known as the Main Tianshan Fault and South Central Tianshan Fault (Allen et al., 1993; Charvet et al., 2011; J. Gao et al., 1998). The western segment consists of the North Tianshan belt, the Yili Block and the South Tianshan belt, separated by the North Tianshan Fault and Nalati Fault, respectively (Han & Zhao, 2018).

The North Tianshan belt (NTS) is an accretionary complex, composed of Carboniferous deep-water sedimentary and volcanic-sedimentary rocks associated with minor ophiolitic fragments (BGMRX, 1993; Dong et al., 2006; B. Wang et al., 2006; Z. H. Wang et al., 2003). Plagiogranite from the ophiolitic fragments was dated at ca. 340 Ma and exhibited subduction-related geochemical characteristics (Dong et al., 2006; C. Li et al., 2014a). The NTS accretionary complex was intruded by voluminous late Devonian to early Carboniferous plutons that have been considered as products of arc magmatism attributed to a southward subduction of the Junggar Ocean (C. Li et al., 2014a; B. Wang et al., 2006). The NTS is also intruded by late Carboniferous to early Permian A-type granite plutons interpreted as post-tectonic magmatism (Han et al., 2010).

The triangle-shaped Yili Block (YB) is sandwiched between the North Tianshan belt and South Tianshan belt (Figure 1b). Its central part is covered by Mesozoic to Cenozoic sediments, while its Mesoproterozoic basement is formed by high-grade meta-sedimentary and meta-volcanic rocks exposed along its northern and southern margins (BGMRX, 1993; J. Gao et al., 1998; J. L. Li et al., 2009; B. Wang et al., 2014a). Two parallel magmatic belts with ages of 460-395 Ma and 375-310 Ma, developed along its northern and southern margins, respectively (Huang et al., 2020). These two magmatic belts were interpreted as reflecting arc magmatism formed due to subduction of the Junggar Ocean and the South Tianshan Ocean beneath the northern and southern margins of the YB, respectively (Huang et al., 2013b; S. H. Yang & Zhou, 2009; Zhong et al., 2017).

The Central Tianshan belt (CTS) mainly crops out at the eastern segment of the Chinese Tianshan Mts (Figure 1b), and it has a Proterozoic basement predominantly consisting of orthogneiss, paragneiss, quartzite, schist, amphibolite and marble (BGMRX, 1993; Hu et al., 2000; X. S. Wang et al., 2017c). While it has been suggested that the CTS is an eastern extension of the YB (e.g., J. Gao et al., 2009) or shows a strong affinity to the YB in terms of zircon U-Pb age patterns (Huang et al., 2015b, 2016, 2017), distinctly different geological records from the Precambrian to Ordovician between them indicate their different origins (Rojas et al., 2014; X. S. Wang et al., 2017c). Alternatively, other authors considered the basement of the CTS as a drifted portion of the northern Tarim Craton due to similar detrital U-Pb zircon age patterns (Ma et al., 2012a, 2012b). The Precambrian basement in the CTS is overlain by Ordovician-Silurian shallow marine meta-sedimentary rocks (P. F. Li et al., 2020; Shu et al., 1999, 2010). Lower Carboniferous limestone, sandstone and siltstone beds unconformably cover the older lithological units (Carroll et al., 1995; Charvet et al., 2007). The CTS records two main magmatic events, exemplified by the Ordovician to Devonian S- and I-type granitic magmatism and Permian A-type granitoids, respectively (Dong et al., 2011). The earlier magmatic event has been interpreted as a result of arc activity, while the latter one is considered as post-orogenic magmatism (Chen et al., 2015; Dong et al., 2011; Shi et al., 2007).

The ~2,500 km long, W-E-trending South Tianshan belt (STS) was traditionally interpreted as an accretionary complex bearing scattered Paleozoic ophiolite mélanges (Alexeiev et al., 2015; Jiang et al., 2014; Xiao et al., 2013). However, significant differences between the eastern and western STS suggest the heterogeneous nature of this unit. Its eastern part is mainly composed of Upper-Silurian to Upper-Carboniferous low-grade to none-metamorphosed shallow water carbonates and siliciclastic (Figure 1c; Alexeiev et al., 2015; Biske et al., 2012; Xiao et al., 2013). In contrast, nearly complete Paleozoic deep-water sedimentary sequences were identified in the western STS (Alexeiev et al., 2015; Lee, 1985). Moreover, the eastern STS preserves granulites and migmatites attributed to a ca. 390 Ma high-temperature (HT) metamorphic event (P. F. Li et al., 2020; L.

J. Mao et al., 2015; Shu et al., 2004; X. S. Wang et al., 2014b; L. Zhang et al., 2016), whereas the western part preserves ca. 320 Ma eclogites and blueschists suggesting (ultra)high-pressure ((U)HP) subduction related event (J. Gao et al., 1995; Lin et al., 2009; Lü & Zhang, 2012; Mühlberg et al., 2016; Tagiri et al., 1995; L. F. Zhang et al., 2002).

3. Geological Overview of the Study Area

3.1. Overview of the Kuruktag Area

The Kuruktag area located at the NE part of the Tarim Craton (Figure 1c) preserves the basement rocks represented by Neoarchean tonalite-granite assemblage with zircon U-Pb ages of ca. 2.7–2.6 Ga, which are locally surrounded by Paleoproterozoic metasediments of the Tuogelakebulake and Xingditage groups (BGMRX, 1993; X. P. Long et al., 2011b; C. L. Zhang et al., 2012a). These rocks were affected by a late-Paleoproterozoic thermal event evidenced by the presence of a large number of metamorphic zircons dated at 1.9–1.8 Ga (C. L. Zhang et al., 2012a). The Paleoproterozoic metasediments were unconformably overlain by Mesoproterozoic sediments of the Yangjibulake and Aierjigan groups equilibrated at greenschist facies conditions. This unconformity was considered as a sign of a ca. 1.9 Ga tectonic event (X. P. Long et al., 2012). The Neoproterozoic Kuruktag Group overlies all above-mentioned units and is composed by pyroclastic rocks and red bed type silici-clastics (Xu et al., 2005; C. L. Zhang et al., 2013). The region also preserves the record of several Neoproterozoic magmatic pulses including ca. 820-800 Ma ultramafic-mafic-carbonatite complex and granite, ca. 780-760 Ma ultramafic-mafic dyke swarm, ca. 740-735 Ma bimodal volcanic series and 650-630 Ma mafic dykes and granitoids (Ge et al., 2012b; X. P. Long et al., 2011a; C. L. Zhang et al., 2012b; W. B. Zhu et al., 2008). Precambrian metamorphic rocks were intruded by early Paleozoic gabbro and granitoid plutons and dykes (Ge et al., 2012a; Liang et al., 2019; Qin et al., 2016).

3.2. Geology of the Mapping Area

In this study, we carried out detailed geological and structural mapping in a 60 km^2 large area near Korla city, in the westernmost portion of the Kuruktag area (Figure 2a). Two sub-parallel NW-SE-trending faults pass across the mapping area. The 50–100 m wide Xinger Fault in the north extending more than 300 km to the east represents a major tectonic boundary separating northern Tarim from the northerly STS as cited above. The subordinate one in the south roughly divides the mapping area into northeastern (NE) domain and southwestern (SW) domain (Figure 2a).

Although both the NE and SW domains consist of gneiss, biotite schist, quartzite, marble and amphibolite, the NE domain exhibits lower metamorphic grade compared to the SW one. On the basis of their lithological and metamorphic features, the SW and NE domains are compositionally comparable to the Paleoproterozoic Xingditage Group and hanging wall Mesoproterozoic Yangjibulake Group, respectively (BGMRX, 1993; Z. J. Gao et al., 1993). However, due to later deformation, these two groups are laterally juxtaposed so that they are collectively called the Korla complex (Ge et al., 2014b).

Paragneiss and biotite schist are the main lithological components of the SW domain. Their protoliths have a maximum depositional age of 2.0 Ga, which were further affected by 1.9–1.8 Ga metamorphic (Ge et al., 2013; C. L. Zhang et al., 2012a). In addition, metamorphic zircon U-Pb ages of ca. 830-800 Ma were also reported for the amphibolite, which occur as blocks/boudins in the schist (Ge et al., 2016). Apart from the migmatitic paragneiss and biotite schist, the study region consists of marble, quartzite, amphibolite, granitoid and gabbro intrusions. The migmatites are represented by meta- and dia-texites. Diatexites often contain abundant centimeter- to meter-scale biotite-rich schollen. These migmatite rocks are mapped as a separate migmatite unit in this study (Figures 2a and 4b).

The NE domain commonly contains more meta-igneous rocks compared to the SW domain. The meta-igneous rocks present in form of orthogneiss or amphibolite have protolith ages dated at 2.65–2.30 Ga or rarely at 1.84 Ga (X. P. Long et al., 2010b, 2012). These rocks also bear 2.0–1.8 and 0.8–0.6 Ga metamorphic zircons (Ge et al., 2016). Quartzite and/or calcareous sandstone are commonly interlayered with marbles.

The study area was also intruded by abundant Paleozoic granitoid and gabbro intrusions dated at 420-400 Ma (Figure 2a) and minor Neoproterozoic granitoids and gabbro dykes (Ge et al., 2012a, 2012b; Qin et al., 2016;

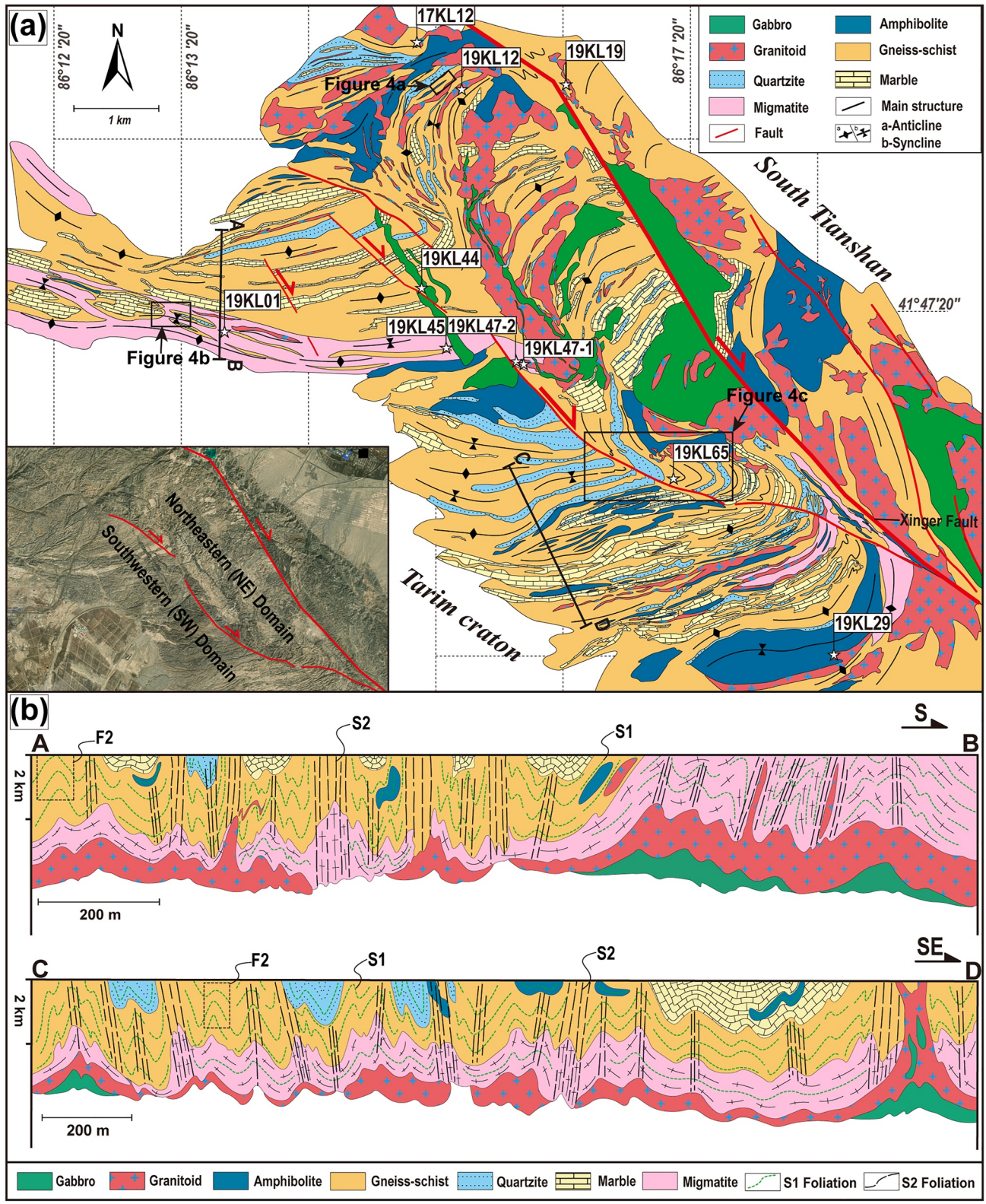

Figure 2. (a) Geological map of the study area, orientations of main foliation and folds are indicated (location in Figure 1c). Geochronological samples are also indicated. (b) Interpretative cross-sections (A-B and C-D) show main deformation features of the study area.

Xu, Zou, et al., 2013). The Paleozoic granitoids are predominantly represented by granite and granodiorite, with meta-aluminous to per-aluminous compositions (Ge et al., 2014b). They are characterized by low MgO, Cr, and Ni contents, and enrichment in Rb, K, U, and relative depletion of Nb, Ta, Ti, P concentrations, as well as dominantly negative zircon $\varepsilon_{Hf}(t)$ values (Ge et al., 2012a, 2014b; Guo et al., 2013; G. P. Liu et al., 2021). Pene-contemporaneous gabbro form either kilometer-scale circular bodies or tens of meters wide dykes across the mapping area. The gabbro have high Al_2O_3, CaO, $Mg^{\#}$, and low P_2O_5, TiO_2, belonging to the calc-alkaline series (Guo et al., 2020; Liang et al., 2019; Qin et al., 2016). They are enriched in large ion lithophile elements (LILE), such as Rb, Ba, K, Sr, but relatively depleted in high field strength elements (HFSE), such as Nb, Ta, P, and Ti (Liang et al., 2019; Qin et al., 2016), and show dominantly positive zircon $\varepsilon_{Hf}(t)$ values (Ge et al., 2014b; Qin et al., 2016). These features led some authors to suggest that the gabbro was derived from the lithospheric mantle wedge with influx of subduction-related fluids/melts (Ge et al., 2014b; Liang et al., 2019; Qin et al., 2016).

4. Structural Descriptions

Detailed geological and structural mapping were conducted together with petro-structural microscopic analysis. The results are presented in a geological map, interpretative cross-sections in Figures 2a and 2b and several detailed structural maps in Figures 3 and 4. The deformational features across the region are summarized as follows.

4.1. The SW Domain

Three episodes of deformation were recognized in the region, designed as D1, D2, and D3. The D1 deformation episode is characterized by a penetrative and ubiquitous metamorphic foliation (S1) in gneiss and biotite schist (Figure 3) defined by alternation of biotite-rich and quartz-feldspar layers (Figure 5a). Both the quartzite and marble developed significant S1 foliation defined by flattening of mineral grains and grain size variations (Figure 5b). In migmatitic paragneiss, the S1 is defined by lit-par-lit alternation of quartz-feldspathic leucosome and garnet, biotite and sillimanite melanosome (Figure 5c). No mineral lineation can be identified on the S1 surface. Micro-is observation further indicates that S1 foliation in migmatitic gneiss usually contains sillimanite, cordierite, garnet, plagioclase, biotite, K-feldspar and quartz (Figures 6a–6c). The sillimanite and biotite, ranging from several millimeters to centimeters in size, show strong preferred orientations and are aligned parallel with the S1 foliation in paleosome and mesosome layers (Figures 6a and 6b). On the other hand, the cordierite ranging in several millimeters in size is generally randomly distributed (Figure 6c). Euhedral crystals of biotite and plagioclase commonly show shape preferred orientation in leucosome layers parallel to mesosome and paleosome fabric without any plastic deformation and/or recrystallization (Figure 6d).

The second episode of deformation (D2) is expressed by heterogeneous folding of regional S1 foliation by upright open to close F2 folds, centimeters to tens of meters in size (Figure 2b). In low-strain domains, the folded S1 foliation was rotated into moderately dipping to vertical attitudes (Figure 5d). F2 folding produces alternations of synforms and antiforms defined by folded quartzite-marble layers and paragneiss that produces visible regional layering in the map view (Figures 4a and 4b). In most cases, the F2 folds show sub-horizontal hinges and sub-vertical axial planes, advocating for sub-horizontal attitudes of the S1 foliation prior to D2 (Figure 3b). In the high-strain domains, tightly folded S1 is nearly completely transposed by steep S2 foliations parallel to F2 axial planes of upright folds preserved in the low-strain domains (Figure 5e). Sometimes, the S2 foliation bears shallowly plunging intersection lineation L2 (Figures 3b and 5f). In metatexites, the stromatitic layering S1 is folded by symmetrical, upright, open to close harmonic F2 folds similar in geometry (Figure 7a). In the diatexites, the weakly anisotropic leucosome contains numerous cm- to m-scale biotite-rich disharmonically folded schollen of metatexites and restitic paragneiss (Figure 7b). Microstructural observations suggest that the mineral assemblage constituting the S1 foliation remained well-preserved in the low-strain D2 domains but is dismembered and reoriented in the high-strain D2 domains. In the former case, the S1 is folded by F2 micro-folds without recrystallization or growth of new minerals. In the S2 transposition zones, recrystallization of mica and quartz grains occurs leading to the development of a new schistosity.

The D3 is marked by deformation of all previous fabrics by map-scale asymmetric F3 folds (Figures 2b and 3a) leading to variable rotation of S1 and S2 fabrics as illustrated by dispersion of S2 in stereonet in Figure 4c. In general, the long limb of regional F3 fold is nearly E-W striking while NW-SE short limb rotated into N-S

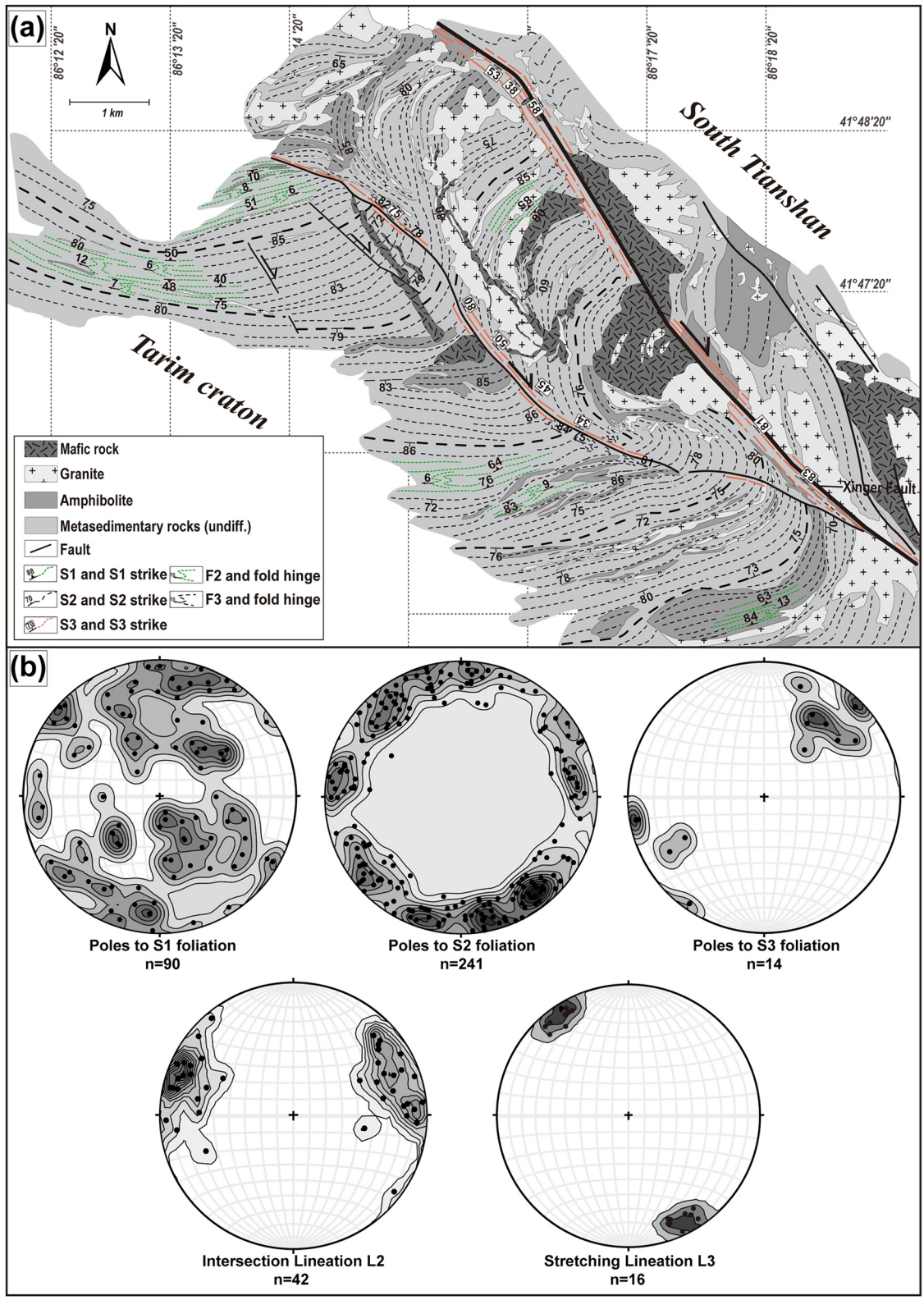

Figure 3. (a) Structural map of planar and linear elements of the Korla area (location in Figure 1c). (b) Stereographic projections of foliations and lineations are shown for the three episodes of deformation (lower hemisphere, equal area).

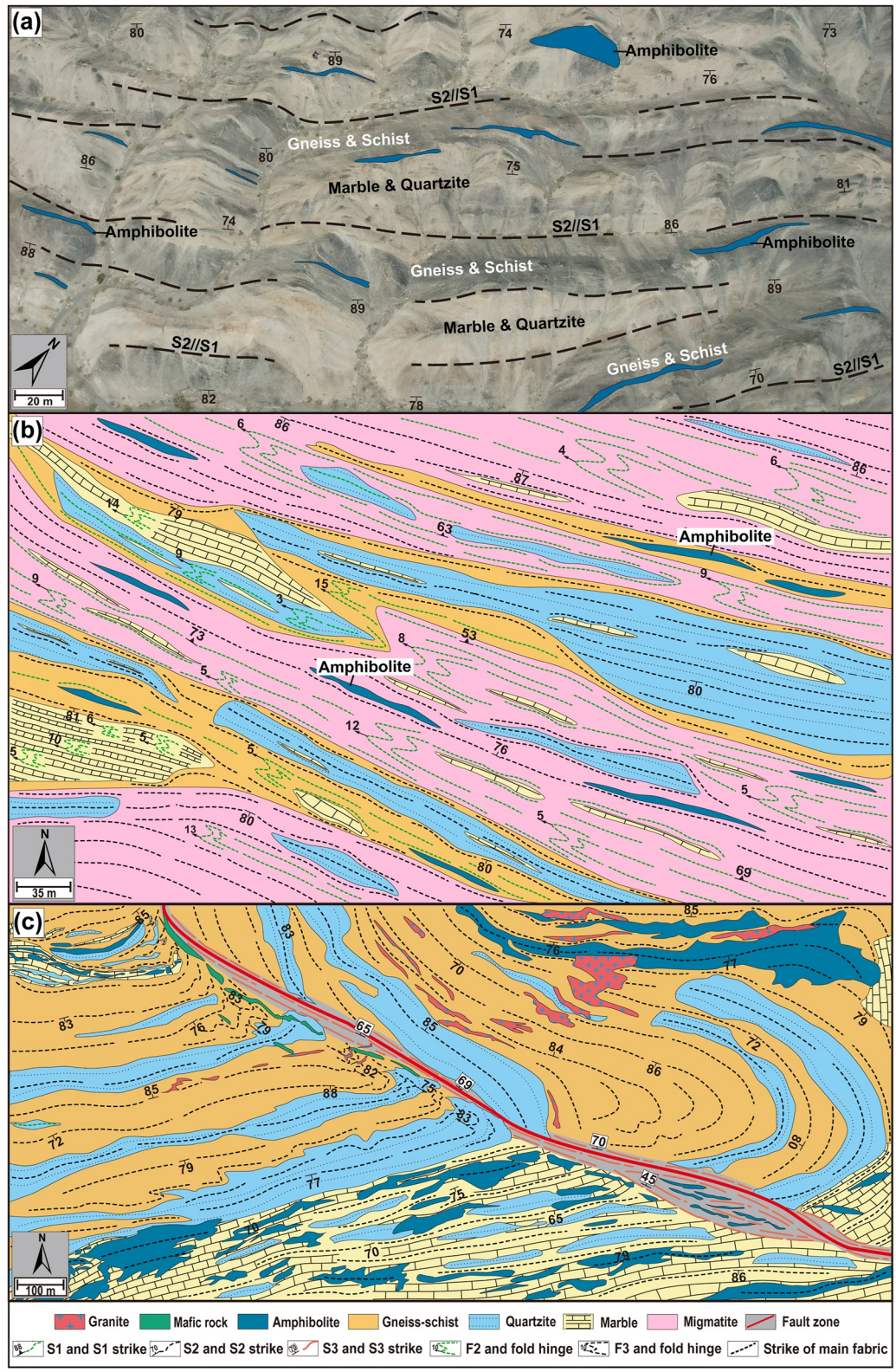

Figure 4. Detailed structural maps of representative areas of the Korla region (Locations are shown in Figure 2a): (a) UAV (unmanned aerial vehicle) image showing alternations of major lithological units in the study area. (b) Geological and structural map showing relations between S1 and S2 fabrics. (c) Geological and structural map showing effects of D3 on the pre-existed fabrics.

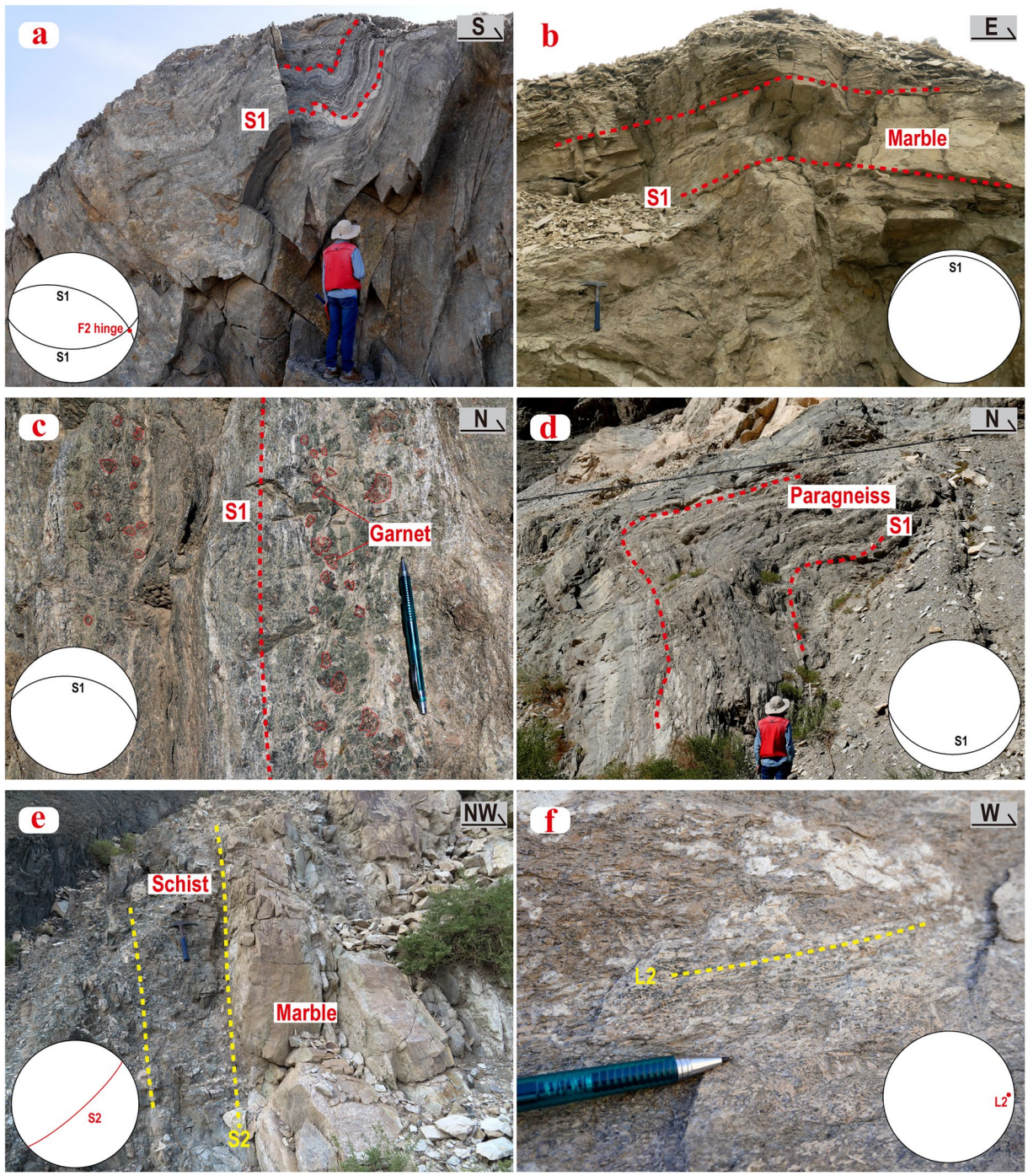

Figure 5. Field photographs illustrating typical structural features of the SW domain in the Korla area. (a) S1 foliation in migmatitic paragneiss (metatexite) defined by stromatitic layering of leucosome and melansome. (b) S1 foliation preserved in marble. (c) Garnet crystals arranged parallel to the S1 foliation. (d) S1 foliation rotated into vertical position by F2 fold. (e) Sub-vertical S2 foliation developed in biotite schist parallel to the marble layer. (f) Sub-horizontal intersection lineation L2 developed in paragneiss.

direction close to the NW-trending Xinger fault (Figure 3a). Strongly flattened F3 folds usually show sub-vertical NW-SE trending axial planar cleavage and steeply plunging hinges near the fault (Figure 4c).

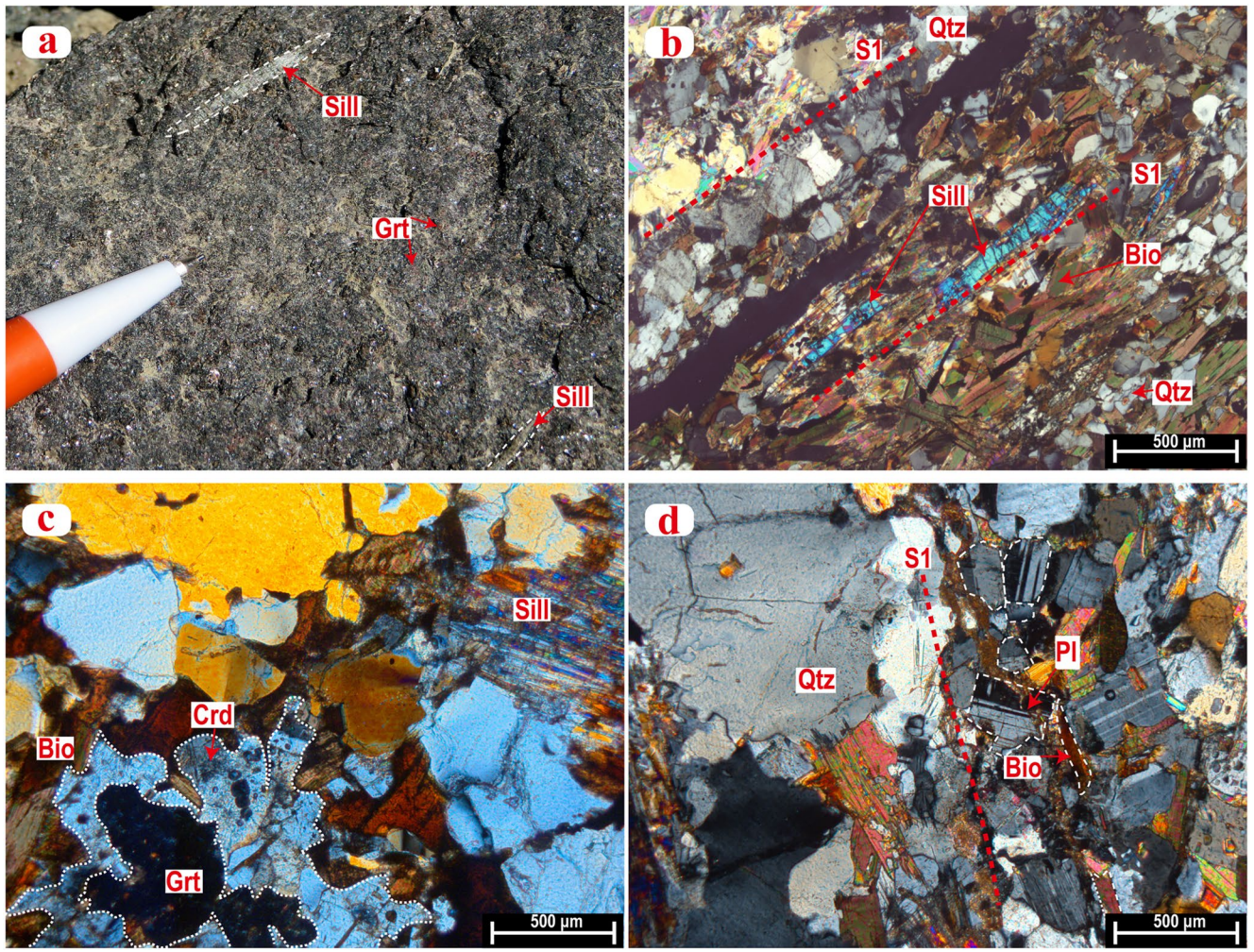

Figure 6. Macro- to micro-petrographic features of paragneiss and migmatitic gneiss from the SW domain of the Korla area. (a) Field photographs showing preferred orientation of sillimanite. (b) S1 foliation in paleosome, defined by preferred orientation of sillimanite and bitotite. (c) Sillimanite, cordierite and garnet preserved in migmatitic paragneiss. (d) S1 foliation in migmatite leucosome, defined by the alignment of euhedral crystals of biotite and plagioclase. Mineral abbreviations: Sill-sillimanite; Bio-biotite; Grt-garnet; Qtz-quartz; Crd-cordierite; Pl-plagioclase.

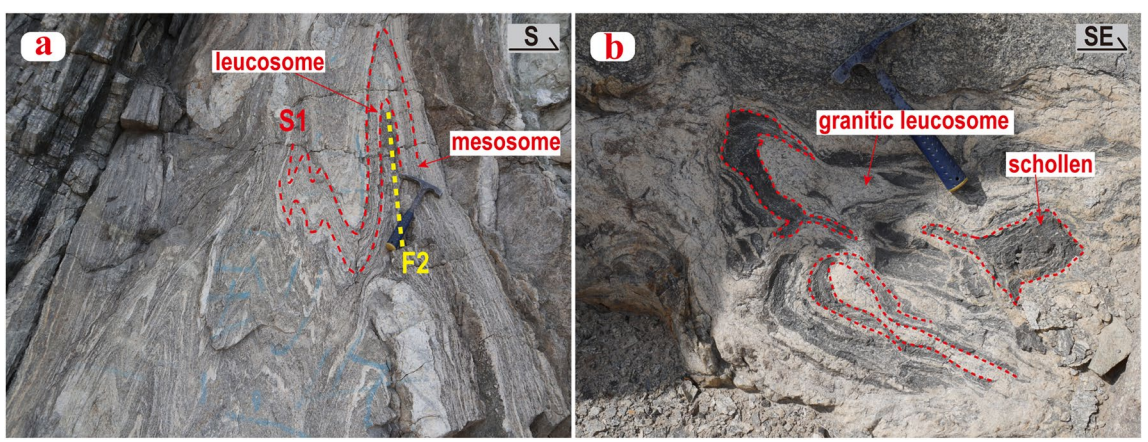

Figure 7. Field photographs of meta- and diatexites. (a) Metatexite stromatitic layering harmonically folded by upright F2 folds. (b) Diatexite containing folded and rotated schollens.

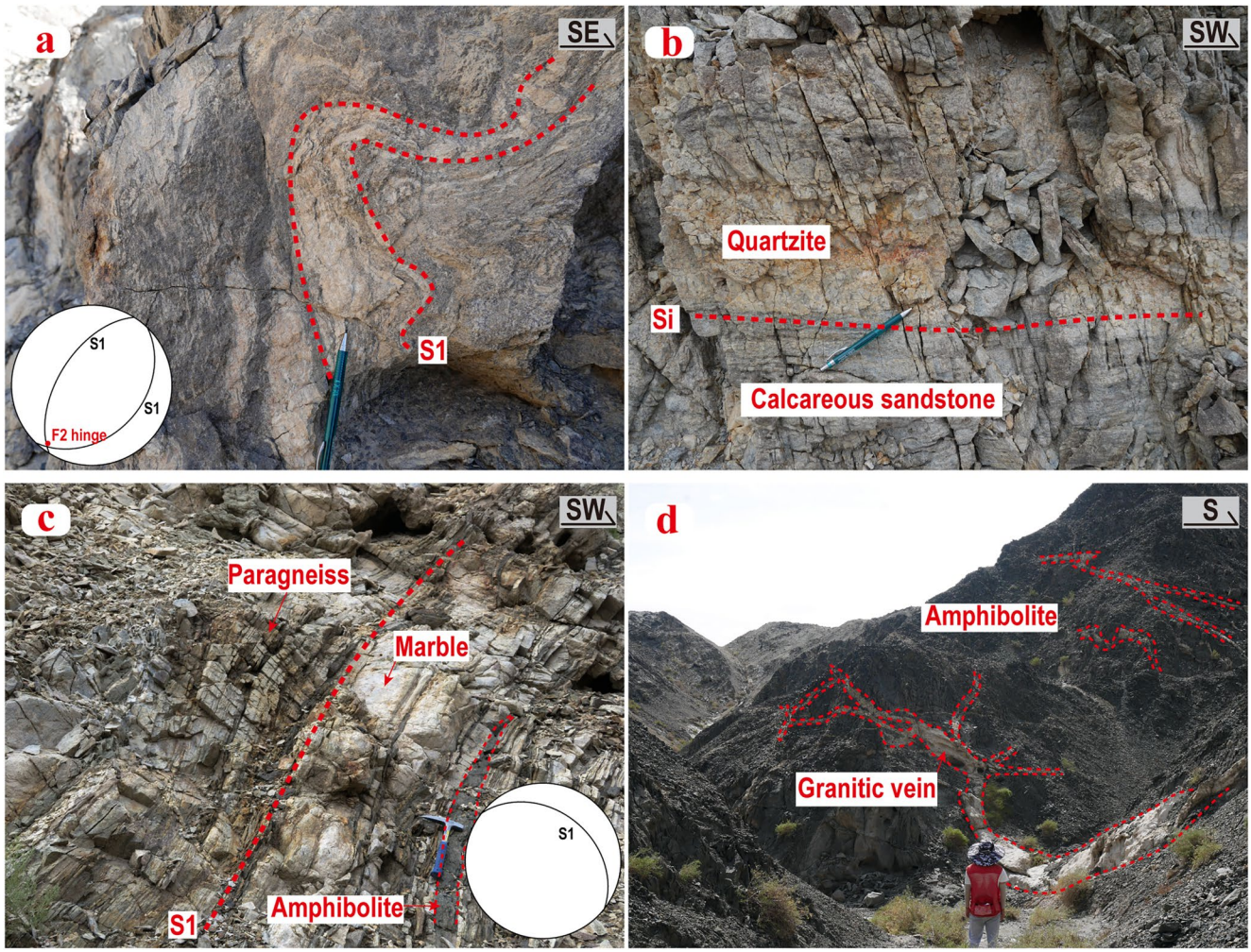

Figure 8. Field photographs of representative structures in the NE domain of the Korla area. (a) S1 foliation in migmatitic paragneiss folded by F2 fold. (b) Undifferenated foliation in calcareous sandstone assigned as Si. (c) Moderately dipping S1 foliation defined by alternations of paragneiss, marble and amphibolite layers. (d) Granitic veins intruded into fractured massive amphibolite.

4.2. The NE Domain

The S1 fabric is mainly expressed by schistosity in biotite schist and stromatitic layering in migmatites. As in the southwest, the originally sub-horizontal S1 fabric is folded by upright, open to close upright F2 folds with horizontal hinges (Figures 8a and 8b). The mineral assemblage of S1 foliation in migmatitic paragneiss is similar to that in the SW domain and it bears garnet, sillimanite, biotite, plagioclase and quartz. By contrast, calcareous sandstone, marble as well as quartzite in this domain commonly preserve less visible variably dipping compositional layering that is generally parallel to S1 schistosity of host paragneiss and schist (Figure 8c). Centimeter-to-meter-wide elongate boudins of amphibolite are preserved within the compositional layering of the host metasediments (Figure 8c). In addition, several meter- to hundreds meter-scale massive and competent amphibolite bodies are fragmented by brittle fractures that are commonly filled by late granite veins (Figure 8d). In general, the NE domain shows similar D3 deformation patterns to that developed in the SW domain characterized by development of map-scale asymmetric F3 folds (Figure 3a) associated with variable rotation of pre-D3 fabrics.

4.3. Strike-Slip Faults

The NW-trending Xinger fault and subordinate fault in the SW are marked by sub-vertical, penetrative, greenschist-facies mylonitic foliation bearing a strong sub-horizontal stretching lineation (L3) defined by

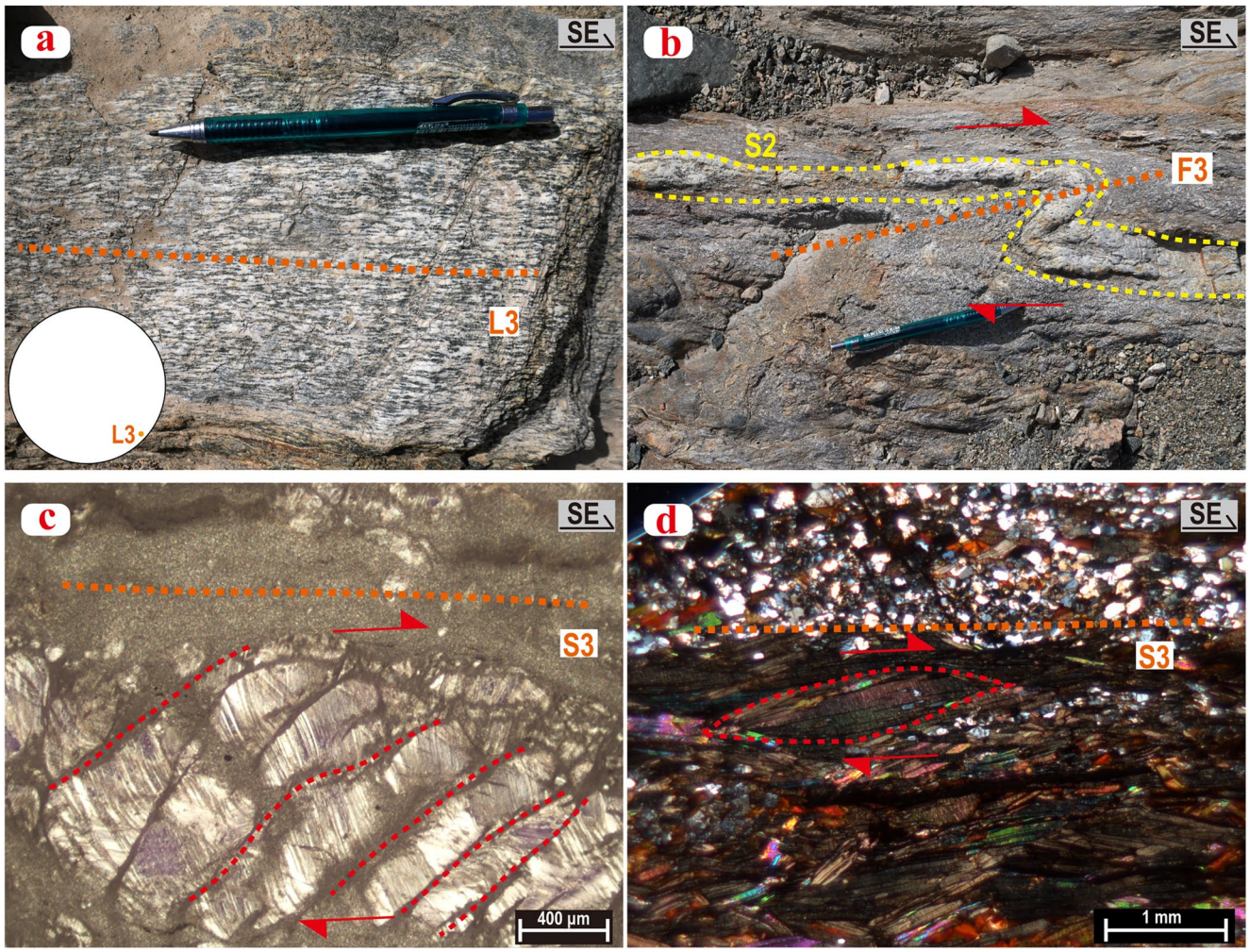

Figure 9. Structural features associated to D3 deformation in the Xinger fault. (a) Sub-horizontal stretching lineation L3 defined by biotite, muscovite, enlongated quartz and feldspar aggregates. (b) Asymmetrical F3 fold indicating a dextral shearing along the fault. (c) Micro-bookshelf faults indicating dextral strike-slip. (d) Mica fish indicating dextral shearing.

alignment of biotite, muscovite, elongated quartz and feldspar aggregates (Figure 9a). Kinematic indicators such as asymmetric folds, micro-bookshelf faults and mica fish indicate a dextral sense of shearing (Figures 9b–9d). Both S2 and verticalized S1 are rotated and attenuated toward a strike of the Xinger fault. These features suggest buckling of S2 due to development of mechanical instabilities close to the fault and subsequent tightening of these folds by shear intensification (Harris, 2003; Platt, 1983). In this regard, the development of the fault activity can be regarded as contemporaneous with the F3 folding.

4.4. Silurian-Devonian Granitoid and Gabbro Intrusions

The study area is intruded by previously dated abundant Silurian-Devonian granitoids and gabbros (Ge et al., 2012a; Guo et al., 2013; Liang et al., 2019; Qin et al., 2016). These intrusions occur either as hundred meters to kilometers plutons or as several meters to hundred meters wide and up to several kilometers' long dykes (Figure 2a). Given that the NE and SW domain show dissimilar metamorphic and deformational patterns, the intrusions exhibit different geometrical relationships with respect to host rock fabrics.

In the relatively lower grade NE domain, granitoid intrusions usually show irregular to semi-elliptic shapes apparently discordant to both S1 and S2 fabrics of the host rocks (Figure 2a). However, when the S2 foliation is strongly developed in the host rocks, the intruded granite apophyses and dykes related to large intrusions show geometries compatible with syn-D2 emplacement. These granite dykes are either parallel to the

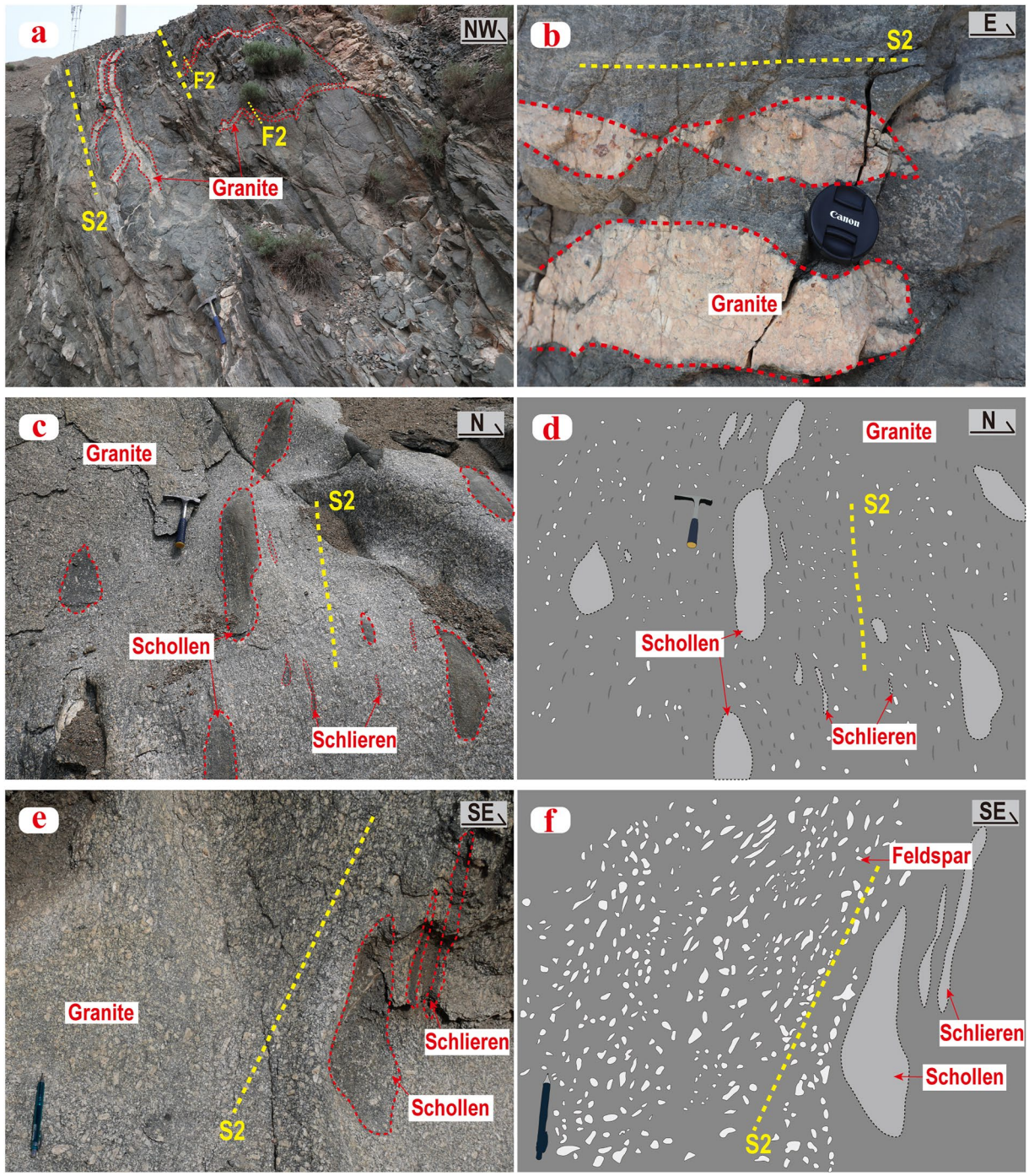

Figure 10. Field photographs of representative structures of granite intrusions from the NE domain of the Korla area. (a) S2-parallel granite sills showing continuity with granite dykes perpendicular to the S2. The latter dykes were also folded and reworked by spaced S2 axial planar foliation. (b) Boudinaged S2-parallel granite sills. (c and d) S2-parallel magmatic fabric defined by the alignment of enlongated schollen. (e and f) S2-parallel magmatic fabric defined by the alignment of coarse feldspar phenocrysts.

S2 foliation or nearly perpendicular to it. The two type of dykes are continuous indicating their synchronous emplacement (Brown et al., 2009). S2-perpendicular granite dykes are often affected by F2 folding that is associated with development of solid-state axial planar cleavage parallel to regional S2 fabric (Figure 10a). On the other hand, the S2-parallel granite dykes are locally boudinaged (Figure 10b). The geometry of granitic dykes described above indicate their emplacement either as axial planar leucosomes (Weinberg et al., 2013) or syn-D2

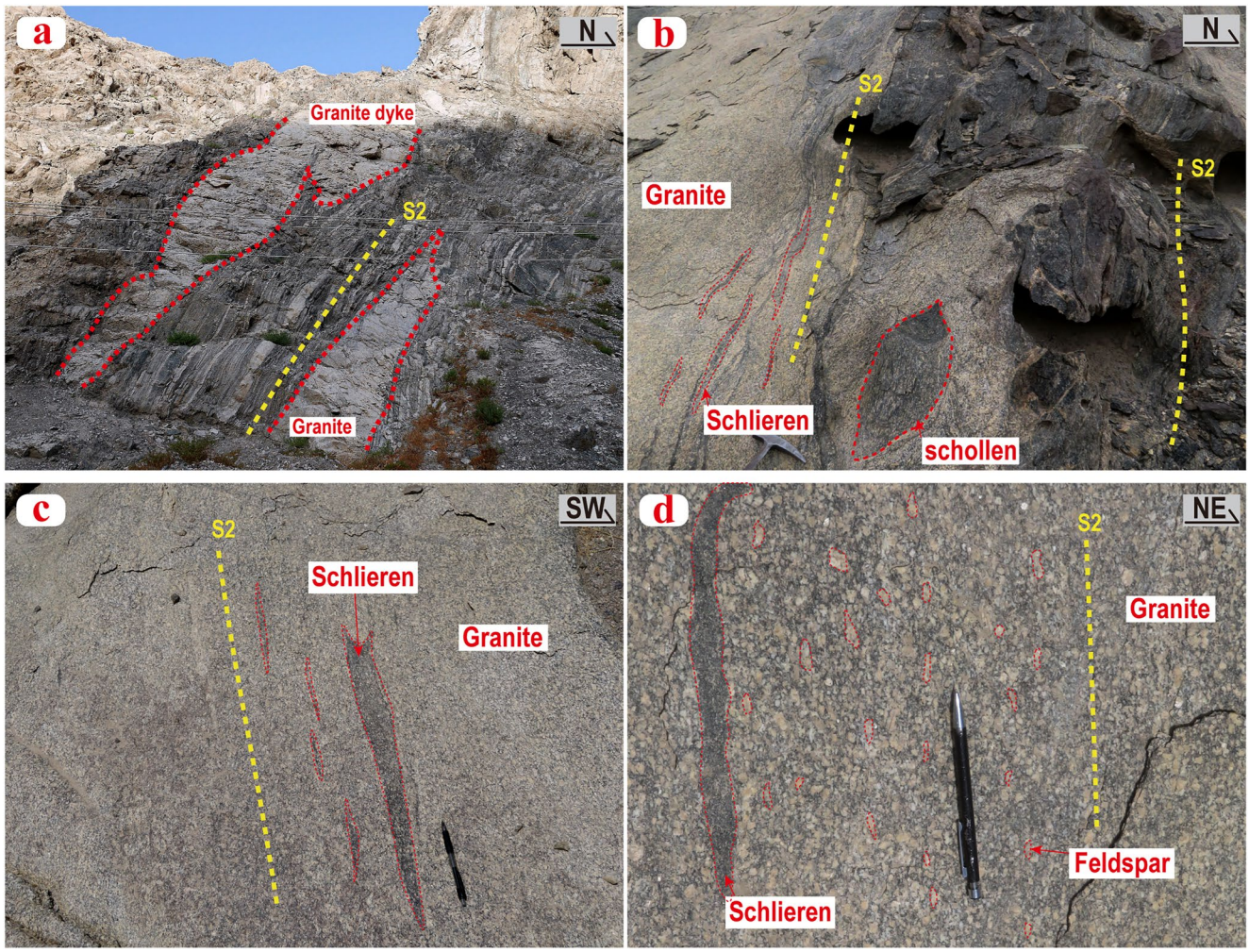

Figure 11. Syn-tectonic granite intrusions related to the D2 deformation in the SW domain of the Korla area. (a) Sheet-like granitic dykes parallel to the S2 foliation of host rocks. (b) Granite show gradual transitional relationship with respect to the surrounding migmatitic gneiss. Schlieren and gneiss schollen are orientated parallel to the main S2. (c) S2-parallel magmatic fabric defined by the alignment of elongated schlieren. (d) S2-parallel magmatic fabric defined by the alignment of coarse feldspar phenocrysts.

tensional fractures. This corroborates the observations from subordinate granite bodies that are associated with migmatites, which commonly show an important magmatic fabric, marked by the alignment of coarse-grained and euhedral feldspars or elongate schollen parallel to the vertical S2 foliation in the surrounding migmatites (Figures 10c–10f).

In the SW domain, the granitoid bodies are generally elongated intrusions or form sheet-like sills parallel to the host S2 fabric (Figure 11a). Less commonly, the granite intrusions are associated with migmatites forming a composite granitoid-migmatite complex (Figure 11b). In these intrusions, a significant S2-parallel magmatic fabric is defined by the preferred orientation of elongate schlieren or euhedral feldspar phenocryst (Figures 11b–11d).

In addition, two NW-trending, dozens of meters wide and 2–4 km long gabbro dykes, with mineral assemblage defined by pyroxene, olivine and plagioclase, are emplaced nearly perpendicular to the regional S2 foliation and F2 fold hinges (Figures 12a and 12b). Such a geometrical relationship implies gabbro dyke emplacement parallel to tensional AC fold fractures, that is, perpendicular to the fold axis and axial plane and parallel to principal compressive stress (Price & Cosgrove, 1990; Stearns & Friedman, 1972). The gabbroic dykes are locally crosscut and displaced by subordinate dextral strike-slip faults (Figure 12a), reflecting impact of the D3 episode on their final geometry.

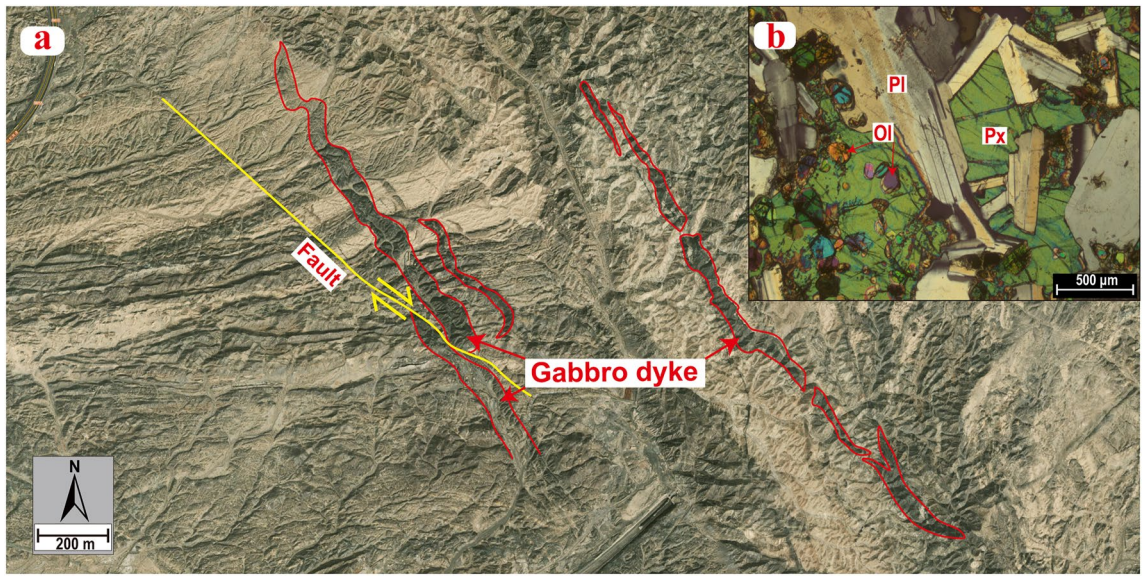

Figure 12. Photographs of the gabbro dykes. (a) Gabbro dykes emplaced nearly perpendicular to the regional S2 foliation and F2 fold hinges. (b) Microphotograph showing plagioclase, pyroxene and olivine in the gabbro. Mineral abbreviations: Pl-Plagioclase; Ol-Olivine; Px-Pyroxene.

5. Geochronological Investigations

5.1. Sample Descriptions and Sampling Strategy

In order to establish age constraints on the polyphase deformation events in the study area, 11 samples were collected from key lithological units for zircon/monazite U-Pb geochronology investigation (see in Figure 2a for locations), including four granite samples (19KL12, 19KL29, 19KL47-1, 17KL12), one gabbro sample (19KL44) and five paragneiss/biotite schist samples (19KL47-2, 19KL65, 19KL01, 19KL45, 19KL19). In addition, one mylonitic granite sample 19KL17 from the Xinger fault was selected for biotite $^{40}Ar/^{39}Ar$ dating. Samples 19KL47-2 and 19KL65 were collected from a migmatitic paragneiss and a biotite schist, respectively. Both of them show well-developed S1 foliation folded by open F2 folds but no signs of D2 transposition. These samples have the potential to date the timing of formation of the S1 fabric. By contrast, paragneiss samples 19KL01 and 19KL45 are characterized by a penetrative, sub-vertical S2 foliation, and therefore can provide age constraints on the D2 event. Two granite samples 19KL12 and 19KL47-1 were collected from the granite intrusions that show S2-parallel shape-preferred orientation of euhedral feldspar phenocrysts in the central part of the intrusion and S2-parallel solid-state foliation at the contact of the granite with the wall rock. These features suggest these granite intrusions probably emplaced syn-tectonically with D2 deformation and therefore the samples can be used to constrain the timing of D2. Two other granite samples 19KL29 and 17KL12 are decimeter-scale sills that were affected by boudinage or F2 folding implying their emplacement during D2 deformation as cited above and are used as proxies of the D2 event. The gabbro sample 19KL44 was collected from an undeformed, tens of meters wide, several kilometers long gabbro dyke that almost perpendicularly crosscuts the host rock S2 foliation. The age of this sample can provide a constraint on the timing of late stage of D2. The biotite schist sample 19KL19 was collected close to the NW-trending D3 fault in the north and displays a penetrative S3 foliation parallel with the fault. The mylonitic granite sample 19KL17 is marked by steeply dipping S3 mylonitic foliation associated with a dextral sense of shear indicators and a sub-horizontal stretching lineation L3 (Figure 9a). These two samples may have potential to provide age constraints on the D3 event.

5.2. Analytical Methods

Zircon and monazite separations were conducted by using standard heavy liquid and magnetic techniques and then selected under a binocular microscope. The selected mineral grains were mounted in epoxy resin and then polished. To reveal the internal zircon and monazite structures, cathodoluminescent (CL) and backscattered electron (BSE) imaging were applied by using an Analytical Scanning Electron Microscope (JSM−IT100) connected

to a GATAN MINICL system at the Wuhan SampleSolution Analytical Technology (WSAT) Co., Ltd., Wuhan, China. These images were further taken as a guide for the selection of suitable portions for the subsequent U-Pb dating.

Zircon U-Pb dating of samples 19KL12, 19KL47-1, 19KL44, and 17KL12 were carried out by using the LA-ICP-MS at the WSAT Co., Ltd. The analyses were performed using a GeolasPro laser ablation system that consists of a COMPexPro 102 ArF excimer laser (wavelength of 193 nm and maximum energy of 200 mJ) and a MicroLas optical system. An Agilent 7700e ICP-MS instrument was used to acquire ion-signal intensities. Detailed operating conditions for the laser ablation system, the ICP-MS instrument and data reduction were described by Hu et al. (2015). The analyses were performed with a beam diameter and frequency of 32 μm and 5 Hz for zircon dating. Zircon 91500 (ca. 1,063 Ma; Wiedenbeck et al. (1995)) and glass NIST610 were used as external standards for U-Pb dating and trace element calibration, respectively. In addition, zircon standards GJ1 (ca. 602 Ma; Jackson et al., 2004) and Plešovice (ca. 337 Ma; Slama et al., 2008) were used as secondary standard to monitor the accuracy of zircon U-Pb dating. Analysis of the secondary zircon standard GJ1 and Plešovice gave weighted mean $^{206}Pb/^{238}U$ age of 606 ± 4 Ma ($n = 8$, MSWD = 0.27) and 333 ± 2 Ma ($n = 8$, MSWD = 0.18), respectively, which are consistent with recommended age within uncertainty. Each analysis incorporated a background acquisition of approximately 20–30s followed by 50s of data acquisition. U-Pb dating of monazite samples (19KL47-2, 19KL65, 19KL01, 19KL45, 19KL29, 19KL19) was performed using the same operating processes and instruments. The spot size and frequency of the laser were set to 16 μm and 2 Hz, respectively. Monazite standard 44,069 (ca. 425 Ma; Aleinikoff et al., 2006) and glass NIST610 were used as the external standard sample for U-Pb dating and trace element calibration, respectively. Monazite standard Trebilcock (ca. 275 Ma; Tomascak et al., 1996) was employed as secondary standard to assess the accuracy of monazite data. Analysis of the secondary standard Trebilcock over the period of analyses yielded weighted mean $^{206}Pb/^{238}U$ age of 277 ± 2 Ma ($n = 20$, MSWD = 2.7), which is consistent with recommended age within uncertainty. An Excel-based software ICPMSDataCal (Y. S. Liu et al., 2008) was used to perform off-line selection and integration of background and analyzed signals, time-drift correction and quantitative calibration. Concordia diagrams and weighted mean calculations were made by using Isoplot (version 4.12, Ludwig, 2003). For both zircon and monazite U-Pb dating, uncertainties on single analysis were reported at the 1σ level; mean ages for pooled U-Pb analyses were quoted at the 2σ level, and these original data are presented in Table S1.

Biotite grains from sample 19KL17 for $^{40}Ar/^{39}Ar$ dating were selected from 30 to 60 meshes crushed rock chips and purified by hand picking under binocular microscope. The selected biotite grains were soaked in thin nitric acid to corrode carbonate, if any. The cleaned samples were wrapped in aluminum foil and put into quartz tubes together with a monitor standard ZBH-2506 biotite ($^{40}Ar/^{39}Ar$ plateau age of 132.7 ± 0.1 Ma; S. S. Wang, 1983). And they were irradiated in the CMRR reactor in Mianyang, Sichuan Province, China. The age determination was conducted utilizing an ARGUS VI® mass spectrometer, at the MOE Key Laboratory of Tectonics and Petroleum Resources, China University of Geosciences (CUG). Details of the analytical procedure are given by Bai et al. (2018). The $^{40}Ar/^{39}Ar$ results were calculated and plotted using the software ArArCALC (version 2.52, Koppers, 2002). A standard air $^{40}Ar/^{36}Ar$ ratio of 298.56 was applied to the calibration, since the extremely high radiogenic Ar with respect to the atmospheric Ar of the biotite sample makes precise determination of initial $^{40}Ar/^{36}Ar$ ratio difficult. Yet, it has been suggested that the initial $^{40}Ar/^{36}Ar$ ratio has little influence on the $^{40}Ar/^{39}Ar$ ages of K-enriched minerals (e.g., biotite; Bachmann et al., 2010; Clay et al., 2011). The data are listed in Table S2.

5.3. Results

5.3.1. Monazite U-Pb Ages for S1-Dominated Paragneiss and Biotite Schist

Monazite grains from the paragneiss sample 19KL47-2 and biotite schist sample 19KL65 show similar features, and they are rounded to stubby in shape, 50–150 μm in size, with homogeneous internal structures. Twenty-three grains from sample 19KL47-2 were analyzed. Nearly all of them gave concordant ages, defining a tight cluster in the concordia diagram, corresponding to a weighted mean $^{206}Pb/^{238}U$ age of 416 ± 2 Ma (Figure 13a). For sample 19KL65, a total of 19 analyses conducted on different grains also formed a tight cluster in the concordia diagram, corresponding to a weighted mean $^{206}Pb/^{238}U$ age of 414 ± 4 Ma (Figure 13b).

5.3.2. Monazite U-Pb Ages for S2-Dominated Paragneiss

Monazite grains from paragneiss samples 19KL01 and 19KL45 show comparable features. They are rounded to stubby shape, and have homogeneous internal structure. Twenty-four analyses on different monazite grains from

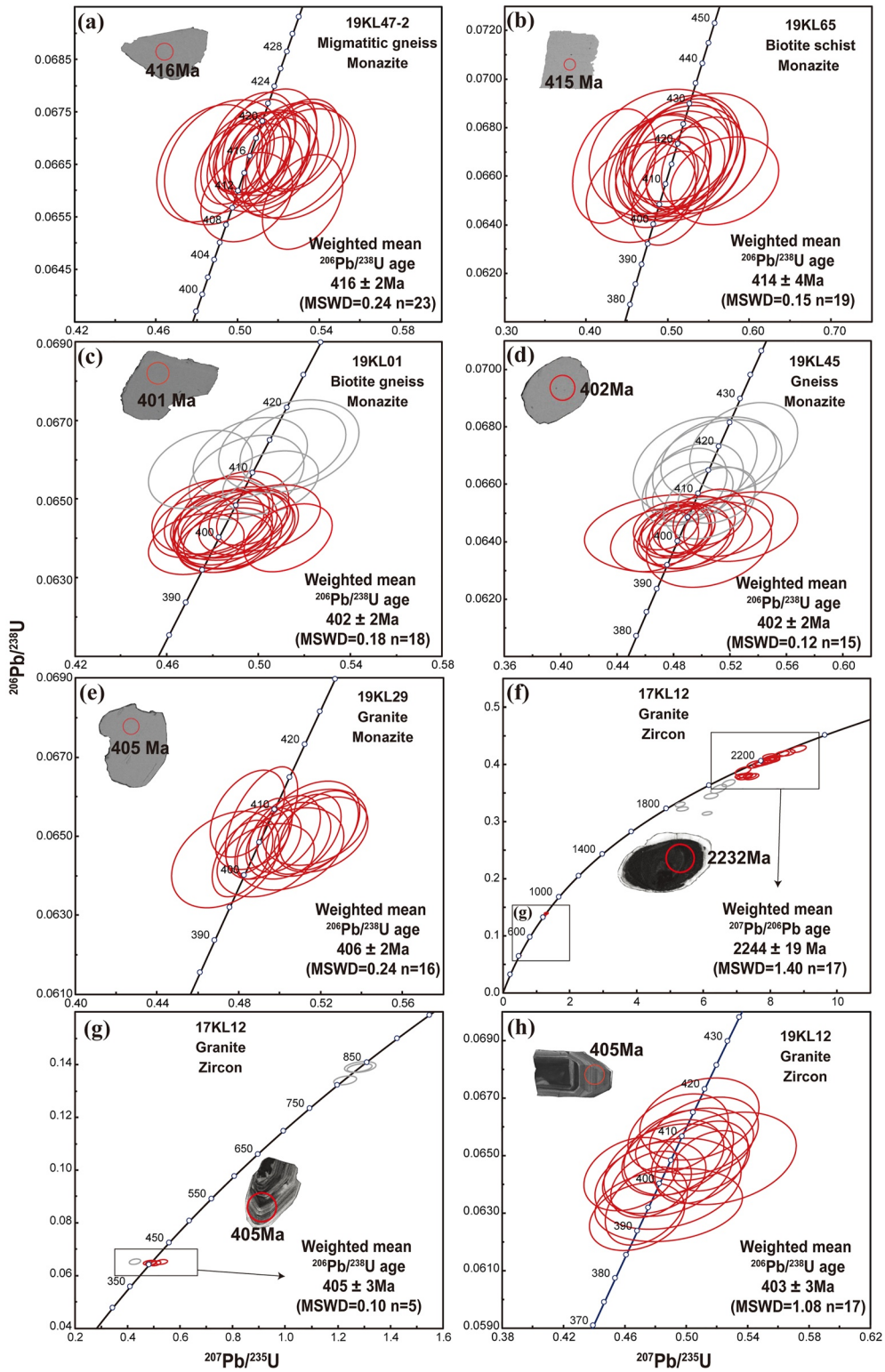

Figure 13. U-Pb concordia diagrams of studied samples from the Korla area, NE Tarim. (a and b) U-Pb concordia diagrams of monazites from S1-dominated gneiss/schist samples. (c–h) U-Pb concordia diagrams of monazite and zircons from S2-dominated gneiss and granite samples. MSWD-mean square weighted deviation. Note that gray error ellipses were excluded for weighted mean age calculation.

sample 19KL01 yielded concordant ages, ranging from 414 to 399 Ma. Among these data, six analyses gave relatively older ages varying from 414 to 409 Ma, a range overlapping with the dominant age populations in the S1-dominated paragneiss cited above. The remaining 18 analyzed spots yielded younger ages clustering around 402 Ma (Figure 13c). Likewise, 24 analyses on different monazite grains of sample 19KL45 yielded concordant ages ranging from 420 to 399 Ma. Among them, 15 grains formed a tight cluster with a weighted mean $^{206}Pb/^{238}U$ age of 402 ± 2 Ma (Figure 13d). The remaining nine analyses yielded older ages varying from 420 to 408 Ma (Figure 13d), similar to the dominated age population in the S1-dominated sample.

5.3.3. Zircon/Monazite U-Pb Ages for Granite and Gabbro Intrusions

Monazite grains from the granitic sill sample 19KL29 are rounded to stubby in shape, 40–120 μm in size, and with homogeneous internal structures. Sixteen analyses were conducted on different grains of the sample. These analyzed spots yielded a unique age population with concordant ages ranging from 409 to 402 Ma, corresponding to a weighted mean $^{206}Pb/^{238}U$ age of 406 ± 2 Ma (Figure 13e). In contrast, 35 analyses on different zircon grains from another granite sill sample 17KL12, gave ages spreading from Paleoproterozoic to Devonian. The Precambrian grains always show rounded shape with length/width ratios of 1:1 to 1:2. In the CL image, they display distinct dark core and bright mantle (Figure 13f). Among them, 17 analyses yielded less concordant ages around 2.2 Ga and three analyses gave concordant ages around 840 Ma (Figure 13f). The remaining six younger zircon grains yielded ages varying from 408 to 403 Ma (Figure 13g). These grains generally show constant Th/U ranging from 0.4 to 0.7 and display concentric oscillatory zoning in their CL images, advocating magmatic origin (Figure 13g). Except for one discordant data point, five analyses on the magmatic zircons defined a cluster with a weighted mean $^{206}Pb/^{238}U$ age of 405 ± 3 Ma, interpreted as the crystallization age of granitic sill (Figure 13g). Samples 19KL12 and 19KL47-1 were collected from other two syn-D2 granite intrusions. The zircon grains from these two samples are prismatic with length/width ratios of 1:1 to 1:3, commonly show well-developed concentric oscillatory zoning, suggesting magmatic origin. Few zircon grains in sample 19KL47-1 have thin, irregular, high-luminescent rims. Seventeen and 25 analyses were conducted on the igneous-related portions of different zircon grains from samples 19KL12 and 19KL47-1, and all analyses gave Th/U ratios ranging 0.3–1.2 and 0.4–1.2, respectively, advocating magmatic origin. Analysis on the magmatic zircons of sample 19KL12 yielded concordant ages and defined a single age population with a weighted mean $^{206}Pb/^{238}U$ age of 403 ± 3 Ma (Figure 13h). For sample 19KL47-1, eight analyses on magmatic zircons yielded relatively older ages varying from 443 to 414 Ma (Figure 14a), and the remaining 17 analyses formed a tight cluster with a weighted mean $^{206}Pb/^{238}U$ age of 404 ± 2 Ma (Figure 14a). Zircon grains from gabbro sample 19KL44 display broad and striped zonation (Figure 14b), suggesting a typical zircon structure of gabbroic rocks (Grimes et al., 2009). Eighteen grains from the sample were analyzed and the related Th/U ratios vary from 0.66 to 1.48, compatible with igneous origin. All analyses in this sample yielded concordant ages ranging from 411 to 394 Ma, defining an age cluster with a weighted mean $^{206}Pb/^{238}U$ age of 405 ± 2 Ma (Figure 14b).

5.3.4. Monazite U-Pb Age for S3-Dominated Biotite Schist

Monazite grains from biotite schist sample 19KL19 have rounded shape with length/width ratios of 1:1 to 1:2 and homogeneous internal structures. Twenty-four grains were analyzed and 16 of them yielded concordant ages spreading from 430 to 374 Ma (Figure 14c). Within these concordant points, five youngest ages defined a tight cluster corresponding with a weighted mean $^{206}Pb/^{238}U$ age of 374 ± 4 Ma (Figure 14c).

5.3.5. Biotite $^{40}Ar/^{39}Ar$ Age of S3-Dominated Mylonitic Granite

$^{40}Ar/^{39}Ar$ data of biotite from the sample 19KL17 formed an increasing staircase-shaped age spectrum at the first five heating steps. However, data from the remaining 15 heating steps at higher temperatures formed a flat plateau corresponding with more than 93.35% of the cumulative ^{39}Ar released, and accordingly, a plateau age of 361.1 ± 2.6 Ma (MSWD = 0.15, Figure 14d) was defined.

6. Discussion

6.1. Polyphase Tectono-Metamorphic Evolution of the NE Tarim

On the basis of structural mapping, it is evident that the penetrative and ubiquitous S1 schistosity, gneissosity, and migmatitic layering preserved in schists, gneisses and migmatites is the main metamorphic fabric in the region. Even though this fabric shows variable attitudes in the field, the upright F2 folding exhibits exclusively

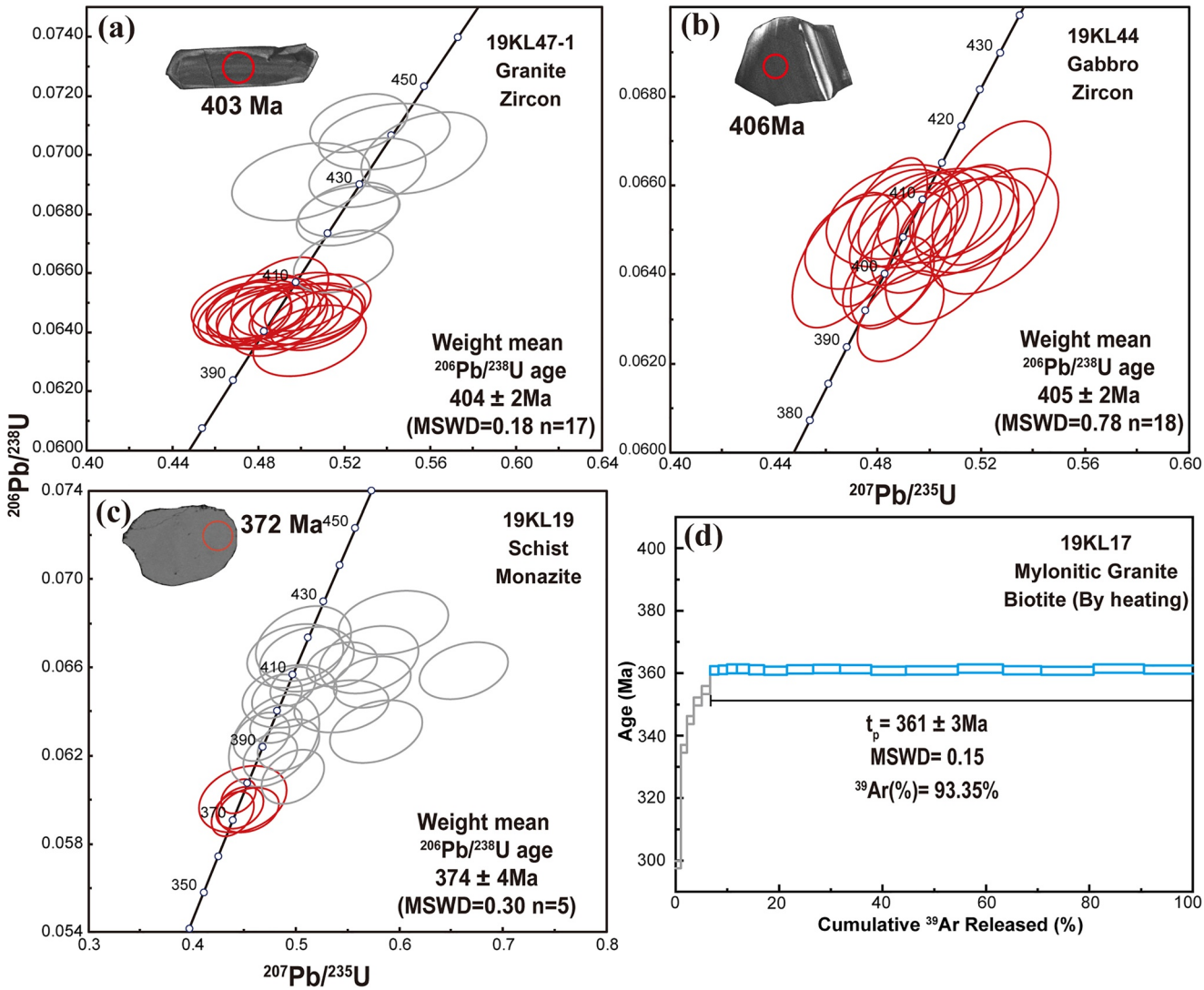

Figure 14. U-Pb concordia diagrams and $^{40}Ar/^{39}Ar$ stepwise heating age of studied samples from the Korla area, NE Tarim. (a and b) U-Pb concordia diagrams of zircon and monazite from syn-D2 granite (19KL47-1) and gabbro (19KL44) samples. (c) U-Pb concordia diagram of monazite from the S3-dominated schist sample 19KL19. (d) Stepwise heating biotite $^{40}Ar/^{39}Ar$ plateau diagram of the mylonitic grantie sample 19KL17. MSWD-mean square weighted deviation. Note that gray error ellipses in figures (a–c) and gray steps in figure d were excluded for the related weighted mean age calculation.

sub-horizontal hinges (Figures 5a and 5b), attesting that the S1 foliation was originally sub-horizontal before D2. This is also supported by sub-horizontal intersection lineation on the S2 foliation (Figure 5f). The widespread presence of S1-parallel leucosome in the paragneiss, attest to at least upper amphibolite-facies metamorphic conditions. However, it remains obscure whether the compositional layering in the lower grade calcareous sandstones, marbles and quartzites, and less commonly (e.g., Si in Figure 8b), some planar fabrics in more competent amphibolite represent the relics of earlier Precambrian metamorphic fabrics. Some of these foliated rocks in the NE domain are crosscut by early Paleozoic granitoids, implying their possible Precambrian origins. However, granites intruding the supracrustal domain are commonly discordant to foliations of any ages and therefore the age of metamorphic fabric in low grade rocks require further investigations.

The effects of D2 deformation are well expressed mainly in the SW domain in paragneiss and biotite schist. There, the D2 event is characterized by open to close upright folds or transposition of S1 by sub-vertical S2 foliation in the high-strain domains (Figures 5d and 5e). In the low-strain domains, the upright F2 folds have steeply dipping axial planes that are parallel to S2 foliation of the high-strain domain. These features suggest that D2 folding resulted from horizontal shortening. By contrast, the more competent amphibolite and quartzite

show exceptionally sub-vertical greenschist facies S2 foliation in the NE domain. In general, the S2 foliation in long limbs of F3 folds strikes nearly W-E, while short limbs are striking in roughly N-S direction (Figure 3a). Given that the mapped area is relatively limited, restoration of the original orientation of S2 foliation prior to D3 deformation is not easy and further mapping of the S2 fabric covering a broader area is required. Nevertheless, similar contractional structures were also documented in the eastern Kuruktag area along the northern margin of the Tarim Craton, 350 km to the east, where intense folds with E-W trending axial planes affect the early Paleozoic strata (Cai et al., 2011).

The D3 deformation is well expressed in the eastern part of the mapped area where it exemplified by the map-view mega-F3 fold and NW-SE trending Xinger fault (Figure 4c). On the basis of kinematic analysis, the D3 related sense of shear criteria indicate dextral strike-slip movement, similar to that described in the eastern segment of the Xinger fault (Cai et al., 2012). These pieces of information suggest that the D3 event was connected with both shortening resulting in F3 folding and shearing parallel to the fault, most likely pointing to a dextral transpression.

6.2. Significance of the Geochronological Data

Substantial Silurian-Devonian ages have been reported in the study area (Ge et al., 2012a; Guo et al., 2013; Kong et al., 2019; Qin et al., 2016), which are broadly overlapping with the geochronological results of the current study. However, these pre-existing data were almost always applied to constrain the timing of magmatic activities, and their relations to the regional metamorphic-structural evolution have been so far not investigated. On the basis of regional deformational evolution and structural positions of the dated rocks, it is possible to provide age constraints of three deformation events reported in this work.

The migmatitic paragneiss samples 19KL47-2 and 19KL65, preserve S1 foliation that is only gently folded by F2. Monazite grains from these two samples gave $^{206}Pb/^{238}U$ ages spread over a range of 418-411 Ma (Figure 15), with nearly identical weighted mean $^{206}Pb/^{238}U$ ages of 416 ± 1 Ma and 414 ± 4 Ma (Figures 13a and 13b). Samples 19KL01 and 19KL45 that exhibit well developed S2 foliation also show a minor group of 420-410 Ma monazite grains. However, the majority of obtained ages in these two samples falls between 405 and 399 Ma (Figure 15), with the same weighted mean $^{206}Pb/^{238}U$ ages of 402 ± 2 Ma (Figures 13c and 13d). Notably, monazites from the S3 dominated sample 19KL19 yielded an even wider age range varying from 430 to 374 Ma. This age range is largely overlapping with the ages of both S1 and S2 dominated samples (Figure 15), except for an additional, younger age population of ca. 374 Ma (Figure 14c).

The oldest and most common age population of 420-410 Ma has the potential to provide age constraints on the D1 event (Figure 15). Given that monazites in migmatite are considered to form during cooling and crystallization of the melts (Morrissey et al., 2014), the weighted mean ages of ca. 416-414 Ma likely represent the youngest age estimates for the main melting period. In this regard, the D1 event associated with partial melting and the related metamorphism could start as early as 420 Ma as indicated by the oldest monazite U-Pb age populations of the samples.

The second main age population of ca. 402 Ma is well expressed by the monazite ages from the S2 dominated paragneiss samples (19KL01 and 19KLL45), and can constrain the timing of D2 event (Figures 13c and 13d). It is noteworthy that the syn-D2 granitoid intrusions as well as dykes and/or sills gave exclusively ca. 406-403 Ma zircon U-Pb ages (Figures 13e–13h) identical to the second main monazite age population cited above. Such a prevailing age population constrains the main stage of D2 compressional deformation at ca. 406-403 Ma (Figure 15). In addition, the gabbro dyke (sample 19KL44) emplaced perpendicularly to F2 fold hinge was also dated at ca. 405 Ma (Figure 14b), similar with the timing of the D2 compression cited above. This probably indicates that the emplacement of gabbro along the syn-D2 tensional AC fracture is related to progressive locking of F2 folds, which also advocates for embrittlement of the whole edifice. One granite sample contains a minor group of 443-414 Ma zircons, which is overlapping with the age of the oldest monazite population (Figures 14a and 15). This probably indicates that regional magmatism had already started during the D1 event. It is noteworthy that only a very small age difference exists between the D1 and D2 events, implying a rapid transition from D1 to D2 probably due to the persistent HT regime developed in the region. The longevity of thermal history is also supported by S1 parallel leucosomes that are in structural continuity with F2 axial planar leucosomes.

Monazite U-Pb ages of the S3-dominated schist (sample 19KL19) and biotite $^{40}Ar/^{39}Ar$ age of the mylonitic granite (sample 19KL17) may provide constraints on the timing of the D3 event. The monazite U-Pb ages are spreading over a range of 424-372 Ma (Figure 15). The oldest ages of 424-411 Ma are comparable with those in

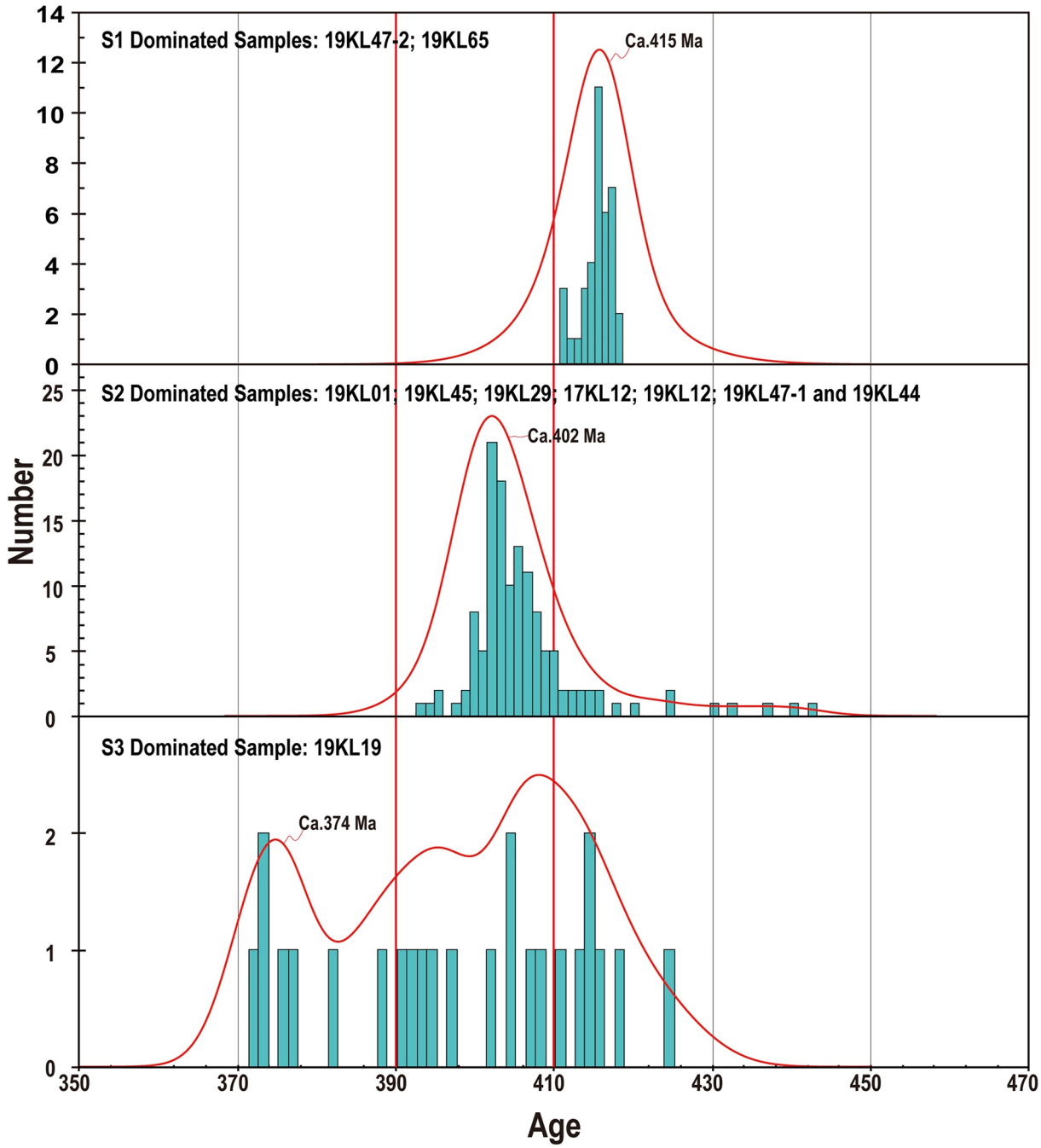

Figure 15. Plots of zircon and monazite U-Pb ages for all analyzed samples with respect to their structures.

the S1-dominated gneiss and schist samples, implying that they recorded the D1 event. The youngest five grains define an age population of ca. 374 Ma, which reflect crystallization of the monazite grains. Given that this age population is only observed in this S3-dominated sample, it most likely represents the timing of F3 folding. The intermediate data of 410-390 Ma unlikely represent the record of the D2 event, even though they are similar to the timing of D2 event discussed above, since no evidence of D2 fabrics is so far recognized in the sample. Alternatively, these ages may reflect partial recrystallization of older, that is, 430-410 Ma, monazites during D3 shearing or mixing of different age domains during the analysis, rather than a true spread of ages.

Biotite $^{40}Ar/^{39}Ar$ dating of mylonitic granite (19KL17) from the Xinger fault gave a slightly younger age of 361 Ma. The fault developed at greenschist facies conditions with deformation temperature approximately

overlapping with the closure temperature of Ar system in biotite, that is, 310–370°C (Grove & Harrison, 1996; Scibiorski et al., 2015). Therefore, the biotite $^{40}Ar/^{39}Ar$ age is interpreted as an age of recrystallization of biotite during the shearing of the Xinger fault. It is noteworthy that ca. 360 Ma mica $^{40}Ar/^{39}Ar$ ages have been previously reported from the Xinger fault in the Kuruktag area, 300 km to the east of study area (Cai et al., 2011, 2012;Z. Y. Zhang et al., 2017). These $^{40}Ar/^{39}Ar$ ages were considered as the timing of shearing of the Xinger fault in the east. Combined with those findings, our data indicate that regional-scale dextral shearing along the Xinger fault developed during the middle-late Devonian. Such a time period is exactly overlapping in age of the D3 folding estimated above, confirming that strike-slip shearing of the region was synchronous with the F3 folding and reinforcing the proposition that D3 deformation was controlled by dextral transpression.

Abundant Proterozoic metamorphic zircon U-Pb ages were previously reported from the studied region (Ge et al., 2014a, 2016; Lu et al., 2008; C. L. Zhang et al., 2012a), and these ages are rarely observed in our zircon samples but never in the monazite samples. We argue that none of the D1-D3 fabrics are of such an age. This suggests that the Proterozoic geological records in the region were significantly erased, in particular in the high-grade rocks. Even the low-grade, less continuous fabrics preserved mainly in the supracrustal part of the NE domain could not be dated in the current, the S1 foliation in the ductile higher-grade region is in geometric continuity with that of low-grade fabric tacitly, implying that the whole region was mainly affected by Silurian-Devonian tectono-thermal event. Similar Silurian-Devonian tectono-thermal reworking of the Precambrian basement rocks has also been recognized in the peripheral terranes near the NE Tarim, in particular in the Dunhuang area. There, the pre-existing Precambrian fabrics are also nearly completely reworked by Silurian-Devonian deformation (Soldner, Štípská, et al., 2022; H. Y. C. Wang et al., 2017a, 2017b; S. Yang et al., 2022).

6.3. Tectonic Implications

6.3.1. Late Silurian-Early Devonian Extension

Sub-horizontal metamorphic fabric has been widely reported in orogenic belts worldwide. This type of structure has been explained either as related to the nappe stacking and crustal thickening as for instance in Norwegian Caledonides or Alpine belt in Europe (Faber et al., 2019; Jeřábek et al., 2012), horizontal channel flow in large hot orogens (Beaumont et al., 2006), or horizontal syn-extensional flow (Cosgrove, 1997). In nappe-stacking or channel flow models, the metamorphic evolution associated with the horizontal fabric always shows HP to middle-pressure metamorphic gradients (Jamieson et al., 2002), whereas in the syn-extensional flow model, the horizontal fabric is generally connected with the low-pressure (LP) metamorphic gradients (Rey et al., 2009; Thompson et al., 2001). In the Korla area, the S1 foliation is associated with development of garnet, sillimanite, K-feldspar and cordierite (Figures 6a–6c). Such an assemblage was suggested to be equilibrated at approximately 840°C/7 kbar, with an abnormally high geothermal metamorphic field gradient of 1200°C/GPa (Guo et al., 2022), typical of LP/HT regime (Brown & Johnson, 2018). These features favor the assumption that the sub-horizontal S1 fabric in the Korla area formed during extensional regime. Coeval with the D1 event, extensive magmatism (including migmatization) was developed in the region as exemplified by the numerous 420-400 Ma granitoids in the region (Ge et al., 2012a; Guo et al., 2013; Qin et al., 2016), suggesting a massive magmatic flare-up, which corroborates a hot geothermal gradient during the late Silurian to early Devonian. Arc-like geochemical signatures of these granitoids suggest that the HT tectonic regime developed in a supra-subduction tectonic environment. The age data show that the formation of the S1 metamorphic fabric and associated magmatism took place at a time period ca. 20 Myr long (Figure 15). Such a long duration of the melting process is common in other supra-subduction orogens worldwide, in particular in circum-Pacific orogenic belts such as the Lachlan orogenic belt in Australia (Collins, 2002a, 2002b; Foster & Gray, 2000; White & Chappell, 1988) or in Cascadia (Hyndman & Lewis, 1995). A common feature in these regions is that the high geothermal gradient is always associated with thinned and stretched lithosphere and elevation of asthenospheric mantle. The presence of early Devonian gabbros in the study area are probably a sign of extreme temperatures related to melting of the mantle, which is a typical feature of lithospheric extension (McKenzie & Bickle, 1988; Wilson, 1993). Given the arc-like geochemical signatures as characterized by enrichment in LILE and depletion in HFSE, the gabbro intrusions were generally considered as typical arc products (Guo et al., 2013, 2020; Qin et al., 2016). However, these mafic rocks are generally younger than the bulk arc-related granitoids in the region (Ge et al., 2012a; Lin et al., 2013), and are not spatially related to them. We argue that features listed above are incompatible with the typical Cordilleras-type continental arcs typified by continuous diorite-tonalite-granodiorite batholiths (Ducea et al., 2003).

Contemporaneous crustal extension was also determined in the neighboring areas of the NE Tarim. For instance, normal faults forming horst and graben structures in late Silurian-Carboniferous strata along the northern Tarim basin were reported 300 km to the south of the study area, indicating that crustal extension started as early as late Silurian (Y. J. Li et al., 2015). Moreover, Silurian successions in the Hongliuhe region, 350 km to the east of the mapping area, gradually switch from polygenetic conglomeratic layers into olistostrome, which was taken as a diagnostic signature for rifting and extension of northern Tarim during the Silurian (Charvet et al., 2007, 2011).

In addition, the Silurian-Devonian extension in NE Tarim is in concordance with coeval extensional regime that governed the tectonic evolution of the neighboring STS and the CTS further to the north (Han et al., 2015, 2016). A systematic comparison of detrital zircons between the CTS and northern Tarim led Han et al. (2015) to propose that the CTS constituted part of northern Tarim in the early Devonian, but soon after split away from Tarim during back-arc opening of the South Tianshan Ocean. A remarkable shift in the Hf isotopic signatures of detrital zircons at ca. 400 Ma from evolved to juvenile in both northern Tarim and the CTS was considered as a sign of significant input of a depleted mantle component compatible with a lithospheric extension (Han et al., 2016; G. P. Liu et al., 2021). In addition, a pronounced early Devonian angular unconformity was recognized in the Bailuntai area of the CTS, and was considered as the signal of crustal extension (X. S. Wang et al., 2020).

The tectonic scenario of opening the South Tianshan back-arc ocean is supported by the following facts: (a) The eastern segment of STS preserves a thick Devonian shallow water Carboniferous carbonate and turbidite sequences, which has been considered to develop in a small oceanic basin (Alexeiev et al., 2015; Allen et al., 1993; Lee, 1985); (b) geochemical characteristics of the ophiolitic rocks in the eastern segment of the STS are compatible with a back-arc environment (Dong et al., 2005; B. Wang et al., 2011); and (c) contemporaneous high temperature metamorphism developed in the eastern STS, exemplified by the ca. 394 Ma Yushugou granulite and extensive ca. 400 Ma migmatization in the Gangou area (P. F. Li et al., 2020; L. Zhang et al., 2016). Taken together, the D1 event in the study area seems to be a response to a generalized extensional regime that affected not only the NE Tarim but also its peripheral units during Silurian-early Devonian.

6.3.2. Middle Devonian Contraction Tectonism

The second tectono-thermal event (D2) in the study area is manifested by the middle Devonian upright folding. Thermal and rheological behavior of the extended and partial molten crust inherited from the D1 stage would strongly influence the rheological conditions of the crust and enable its deformation even at weak stress (Kruckenberg et al., 2011; Rosenberg & Handy, 2005; S. Wang et al., 2021). This is evidenced by presence of F2 axial planar leucosomes and S2-parallel syn-tectonic emplacement of granitic magma (Figures 10b and 10c), which suggest gradual transition from D1 to D2 in the presence of melt.

A km-scale wide, W-E-striking decollement zone developed in the Hongliuhe region 350 km to the east part of the Korla was dated at ca. 383 Ma (muscovite $^{40}Ar/^{39}Ar$), which was interpreted as a timing of important convergence along the northern Tarim margin (Cai et al., 2011). This convergence probably recorded the same contractional deformation as the D2 event in the study area. A contractional tectonic regime was also recognized across the neighboring STS and the CTS further to the north. In the CTS, large-scale tight upright folding associated with the development of a penetrative nearly W-E-striking sub-vertical schistosity was documented and was considered to be associated with sub-horizontal nearly N-S shortening (P. F. Li et al., 2020). The age of deformation was dated by these authors at ca. 356 Ma on the basis of hornblende $^{40}Ar/^{39}Ar$ ages. In the Wuwamen area of the eastern STS, a large-scale fold-and-thrust system was commonly recognized across the belt (Charvet et al., 2007; B. Wang et al., 2018) and this thrusting event was dated at ca. 360 Ma by muscovite $^{40}Ar/^{39}Ar$ method (B. Wang et al., 2011; X. S. Wang et al., 2022). It also has been documented that a in the eastern STS late Carboniferous shallow-marine bioclastic limestones, coarse sandstones, and conglomerates unconformably cover the folded pre-Carboniferous rocks (Chen et al., 1999; Zhou et al., 2001). These data were interpreted as recording a compressional deformation probably of Devonian-Carboniferous time (Lin et al., 2009). Thus, the middle Devonian D2 shortening in the study area seems to be comparable with the contractional deformation developed in the eastern STS and the CTS, implying a generalized compressional regime across the region.

6.3.3. Late Devonian Transpressional Deformation

The late Devonian tectonism is exemplified by the pene-contemporaneous D3 folding and discrete dextral strike-slip shearing typical for transpressional deformation. Dextral shearing in the southern CAOB and northern Tarim has long been thought to be activated in Permian times in response to final amalgamation of the region (e.g.,

Laurent-Charvet et al., 2002; P. F. Li et al., 2020). However, except for the late Devonian dextral shearing reported in the mapping area, coeval dextral shearing was also documented along the Main Tianshan dextral strike-slip fault along the CTS and the Xingdi dextral strike-slip fault along NE Tarim (Cai et al., 2012; Z. Y. Zhang et al., 2017). These dextral shear zones were mainly located along the margin of northeastern proto-Tarim Craton. They may be activated during late Devonian eastward movement of Yili-Turfan-Hami blocks with respect to proto-Tarim Craton (B. Wang et al., 2007a; X. Zhu et al., 2018, 2019b). Indeed, oblique convergence between different terranes is commonly accompanied by transpressional deformation along their irregular margins (Díaz-Azpiroz et al., 2014; Sarkarinejad et al., 2008).

6.3.4. New Perspectives on Silurian-Devonian Geodynamics of the NE Tarim

Based on regional geological records introduced above, it is apparent that the NE Tarim Craton and the northerly STS and CTS experienced comparable early Paleozoic tectonic evolution. When these pieces of geological information are integrated with our data, an updated early Paleozoic geodynamic scenario considering the CTS as a continental arc, the eastern STS as a back-arc basin and northern Tarim as a rifted continental margin is proposed.

The CTS was formerly assumed as an independent block that was separated from the Tarim Craton during the Neoproterozoic (Wu et al., 2022a, 2022b). However, recent investigations on xenocrystic zircons from basement rocks and detrital zircons from Neoproterozoic to early Paleozoic sedimentary sequences from both CTS and northern Tarim exhibited comparable age patterns (Han et al., 2015; Ma et al., 2012a, 2012b; X. S. Wang et al., 2017c). As a consequence, these authors suggested that the two main units were connected at least during Ordovician-Silurian time (Figure 17a). This assertion is further supported by (a) similarities of Ordovician-Silurian conodont and brachiopod species found in the CTS, STS and northern Tarim regions (Rong et al., 1995; Z. H. Wang et al., 2007b) and (b) absence of older than Silurian ophiolites between the CTS and NE Tarim. In these regards, a Tarim-CTS connection during, at least, early Paleozoic time can be established. The widespread early Paleozoic rocks that have calc-alkaline compositions and show arc-related geochemical signatures (Dong et al., 2011; Ge et al., 2012a, 2014b; Guo et al., 2013; Lin et al., 2013; Ma et al., 2014; Shi et al., 2007) across the northern Tarim-CTS region therefore represent products of a broad magmatic arc (more than 200 km wide from south to north) as it is proposed by Han et al. (2015). Such continuous arc magmatism would start as early as ca. 490 Ma and lasted until ca. 300 Ma in the CTS (Figure 16). Notably, the ages of these rocks decrease southward (also inland-ward) from ca. 490 Ma in the CTS to ca. 420 Ma in northern Tarim (Figure 16), probably reflecting the southward motion of the subducted Paleo-Asian oceanic plate over the time. Such a tectonic configuration involving a south-dipping subduction system is in accordance with north-vergent ductile structures documented in the STS (Charvet et al., 2011; J. Gao et al., 1995; Lin et al., 2009; Shu et al., 2002; B. Wang et al., 2008, 2010). When the magmatism was on-going at ca. 420 Ma in the study region, the supra-subduction system was already established ca. 70 Ma ago (Figure 17b). Such a long magmatic activity possibly resulted from vigorous heat input of convecting asthenosphere. This process is responsible for thermal softening and erosion of the overriding continental lithosphere. Modern examples of similar supra-subduction systems are known from both sides of Pacific where the actual subduction zones have 200 to 1,000 km wide upper plate supra-subduction arc-back-arc regions with heat flow reaching 90 mW/m^2 (Currie et al., 2008; Hyndman, 2019; Hyndman et al., 2005).

Until the late Silurian, the thinned and hot supra-subduction crust might form a ductile lower crustal layer that can be easily stretched. This essential prerequisite would eventually give rise to the break-up terminated by spreading of STS back-arc ocean and drifting of the CTS away from the northern margin of proto-Tarim Craton (Figure 17c). Lithospheric extension in the region probably started as early as the late Silurian, as indicated by initiation of late Silurian extensional structures in northern Tarim (Charvet et al., 2007; Y. J. Li et al., 2014b). Meanwhile, the ca. 420 Ma magmatism became abundant along the south part of the South Central Tianshan fault, including the STS and northeastern Tarim Craton (Figure 16). During this stage, the overriding zones of the future back-arc basin experienced high-temperature metamorphism and melting, exemplified by the ca. 395 Ma granulite-facies metamorphism in the current eastern STS (L. Zhang et al., 2016; Zhou, 2004) and the ca. 420-410 Ma high-temperature fabric described in the current study. The period of maximum back-arc spreading was probably associated with continuous crust melting overlapping with emplacement of mafic rocks (gabbro) and subduction-related arc magmatism in the region. The presence of abundant middle Devonian monazites/zircons in the related rocks (Figures 15 and 16) suggests a continuity of a hot supra-subduction regime till at least that time. Such Silurian-Devonian supra-subduction stretching in association with spreading of the STS back-arc basin was probably assisted by switching of subduction system from advancing to retreating regime, similar to

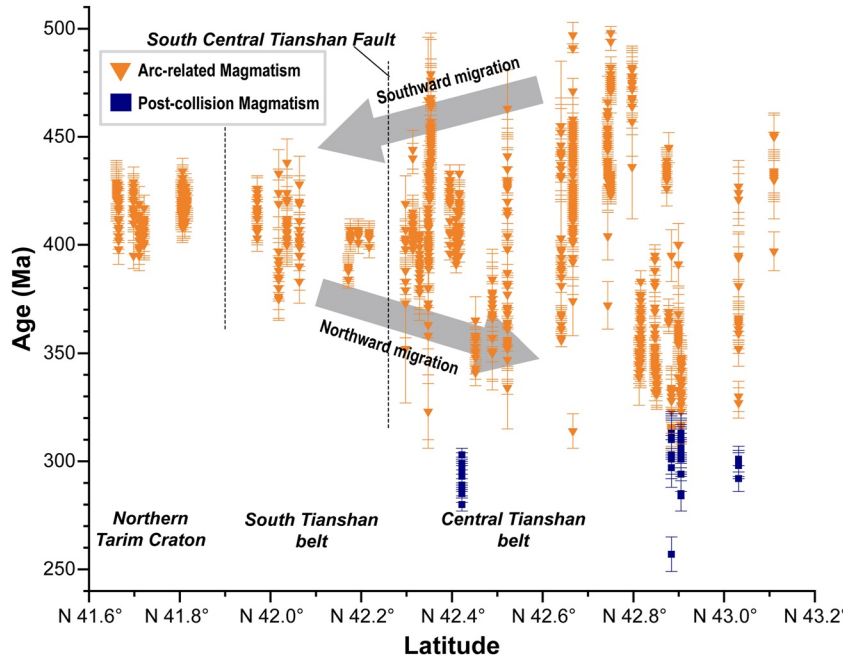

Figure 16. Ages data of the Paleozoic igneous rocks from the NE Tarim, eastern STS and CTS domains. Data are compiled in Table S3: Chen et al. (2012, 2015), Dong et al. (2011), Ge et al. (2012a, 2014b), Huang et al. (2015a), Lin et al. (2013), Ma et al. (2012c, 2014), Qin et al. (2016), Shi et al. (2014), Shi et al. (2007), and Zhong et al. (2015).

that described in Han et al. (2015, 2016). Importantly, the arc magmatism younger than 420 Ma across the Tianshan Mts. shows the northward migration trend from ca. 400 Ma in the northern Tarim to ca. 300 Ma in the CTS (Figure 16). This temporal and spatial variation is compatible with retreating of subduction front further north (Figure 17c). Further west, the development of 386-295 Ma magmatism inside the Yili Block was also considered as a consequence of crustal extension due to northward retreat of the south-dipping Paleo-Asian Ocean subduction system (Cao et al., 2017; J. S. Liu et al., 2022). This is roughly overlapping in time with the retreating subduction proposed in this study, implying possible genetic link between both regions.

The subsequent stage is manifested by regional contraction during the middle Devonian exemplified by horizontal D2 shortening of the northern Tarim margin (Figure 17d). It accounted for unconformable sedimentation of late Carboniferous shallow-marine sediments covering the folded pre-Carboniferous rocks in the STS (Chen et al., 1999; X. S. Wang et al., 2022; Zhou, 2001). This contractional deformation across the region was previously interpreted as recording the closure of the STS back-arc basin and collision of northern Tarim with its northerly peripheral arc system (Cai et al., 2011; Lin et al., 2009, 2013). However, lack of detrital zircons from the CTS in early to late Carboniferous strata in northern Tarim was interpreted by others as an argument for existence of the STS back-arc ocean till at least the late Carboniferous (Han et al., 2015). There are so far no signs (e.g., high-pressure metamorphic rocks) supporting far-traveling continental underthrusting of the CTS beneath NE Tarim. Instead, their mutual interaction is manifested by folding of sedimentary sequences and hot partially molten crust of the NE Tarim margin (Figure 17d). Ge et al. (2012a) and (Lin et al., 2013) proposed that the STS back-arc oceanic crust subducted southward underneath the northern Tarim thereby triggering magmatism during late Silurian-early Devonian in this region. However, this magmatism developed slightly earlier than the opening of the South Tianshan back-arc basin. In addition, some authors suggested that little or no magmatism would be generated as a result of subduction of small-scale oceanic basin because short oceanic slab cannot reach sufficient depth to cause dehydration and partial melting of the overriding mantle (K. Liu et al., 2020; Sisson et al., 2003; Tang et al., 2021). These features suggest that a large-scale subduction of back-arc basin crust cannot be warranted, even the possibility of underthrusting of the South Tianshan back-arc basin crust underneath the northern Tarim during D2 contraction cannot be discarded (Figure 17d). The change of tectonism from the late Silurian to early Devonian extension to middle Devonian contraction is probably related with switching of geodynamics of the supra-subduction system (Collins, 2002a).

10.1029/2023TC007792

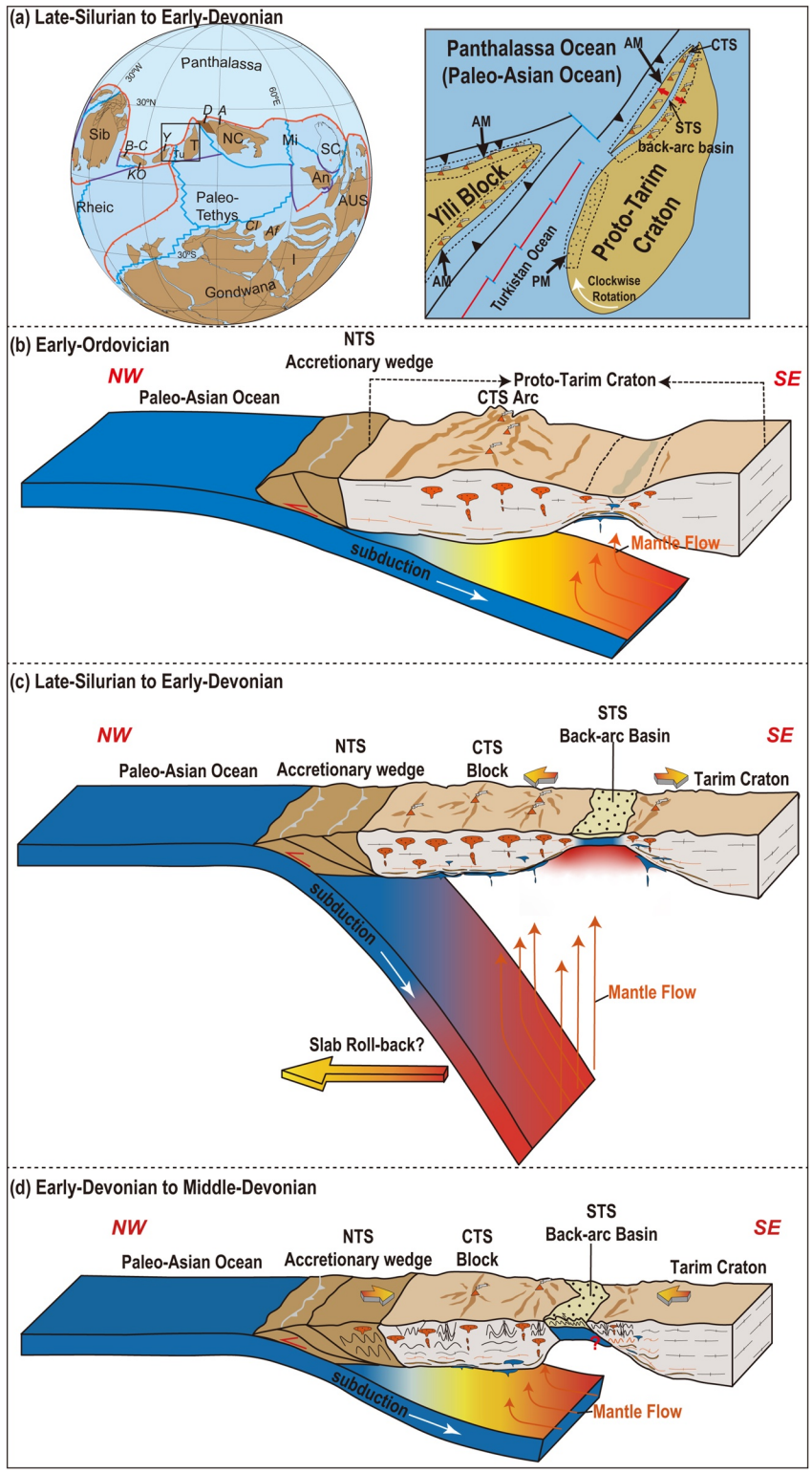

Figure 17. (a) Paleogeographic position of the Tarim with respect to the Kazakhstan-Yili Block during the late Silurian-early Devonian (modified after Domeier (2018)). (b) The proto northern Tarim margin evolved into active continental margin started at the Early Ordovician due to southward subduction of exterior Paleo-Asian Ocean. (c) Splitting of proto northern Tarim margin during the late Silurian to early Devonian gave rise to northward drifting of Central Tianshan continental arc and opening of South Tianshan back-arc basin. (d) A convergent regime governed the tectonic evolution of NE Tarim during the early-Devonian to middle-Devonian. Plate and terrane abbreviations: Sib-Siberia; B-C-Boshekul-Chingiz; KO-Kokchetav; Y-Yili; Tu-Turkistan Ocean; T-Tarim; D-Dunhuang; A-Alxa; NC-North China; Mi-Mianlue Ocean; SC-South China; An-Annamia; AUS-Australia; CI-Acentral Iran; Af-Afghan terranes; I-India; CTS-Central Tianshan; STS-South Tianshan; NTS-North Tianshan; AM-Active Margin; PM-Passive Margin.

We propose that the eastern segment of northern proto-Tarim and CTS was located above a unique south-dipping oceanic subduction, while its western part was still a passive margin (PM). This statement is in agreement with the western STS deep-water sedimentation from Ordovician to early Triassic (Lee, 1985; Wan et al., 2020) contrasting with eastern STS short-lived back-arc basin shallow-water sedimentation (Charvet et al., 2011; Shu et al., 2002; B Wang et al., 2018). This model can be tested against recent full-plate paleogeographic reconstructions for the given time frame (Domeier, 2018). His model shows that starting from 420 Ma, the northeastern margin of the Tarim basement (eastern part of the northern margin in current coordinates) faced subduction of the exterior Paleo-Pacific (Panthalassa) Ocean (Figure 17a). At the same time, the southwestern margin of the Tarim craton (western part of the northern margin in current coordinates) was a passive margin of so-called Turkistan oceanic basin (Figure 17a), which is a remnant of interior Ran Ocean in the Domeier (2018) reconstructions. This is consistent with the idea that the western part of the Tarim Craton was located south of northward dipping subduction of the Turkistan Ocean beneath the Yili Block during the early Paleozoic (Allen et al., 1993; Xiao et al., 2008), while all this system was already subducted by the Paleo-Pacific Ocean from the east (Figure 17a). In these regards, the Domeier (2018) reconstruction satisfies plate triple junction rule and can be also validated by the geological data.

7. Conclusions

Geological mapping, petro-structural observations and geochronological data are combined to characterize the geodynamic evolution of the eastern segment of northern Tarim during the early Paleozoic. The principal conclusions are.

1. Three main deformational-metamorphic fabrics were recognized in the Korla area of the NE Tarim Craton: the S1 is exemplified by a sub-horizontal, high temperature/low pressure metamorphic foliation, in part associated with migmatization, interpreted as a consequence of extension; the S2 is represented by steep axial planar foliation of regional upright F2 folds that was connected with nearly sub-horizontal shortening; and the S3 is marked by spaced, NW-SE-striking foliation associated with transpressional deformation that resulted in dextral shearing and mega-folding of S1 and S2 fabrics in the region.
2. The development of the S1 fabric initiated at 420 Ma or earlier, and lasted till 410 Ma, the D2 event corresponding with formation of S2 fabric was activate mainly from 410 Ma till 380 Ma, and the D3 transpressional deformation took place during the late Devonian around ca. 370-360 Ma.
3. The eastern segment of proto northern Tarim margin probably evolved into a supra-subduction environment during the early Paleozoic. Lithospheric extension of the supra-subduction system during late Silurian-early Devonian resulted in stretching and thinning of the crust associated with HT/LP metamorphism and crustal anatexis. Further stretching of the northern Tarim Craton would eventually lead to northward drifting of Central Tianshan continental arc and opening of South Tianshan back-arc basin. The region was further affected by contractional deformation during the middle Devonian. During the late Devonian to Permian, the northeastern proto-Tarim Craton was affected by transpressional deformation probably induced by the oblique convergence between the Tarim Craton and its northerly terranes.

Acknowledgments
This project was supported by the National Natural Science Foundation of China (42372240, 42022017, 42021002), the International Partnership Program of Chinese Academy of Sciences (No. 132744KYSB20190039) and the project from Guangdong Province (2019QN01H101). A funding from Grant Agency of the Czech Republic (GAČR) project 19-27682X to K.S. is also acknowledged. Stephen Collett is thanked for editing the earlier version of this manuscript. We appreciate Kang Xu, Tan Shu, Ming Xiao and Lingzhu Kong for their kind assistance during the field investigation and experimental analysis. We are indebted to the editor and two reviewers for the constructive reviews and valuable comments that improved manuscript.

Data Availability Statement

All original data used in this paper are available in Tables S1–S3. The data reported in this paper are available in the Mendeley Data Repository: https://doi.org/10.17632/xdhxyk6yvh.2 (Ning & Jiang, 2023).

References

Aleinikoff, J. N., Schenck, W. S., Plank, M. O., Srogi, L., Fanning, C. M., Kamo, S. L., & Bosbyshell, H. (2006). Deciphering igneous and metamorphic events in high-grade rocks of the Wilmington Complex, Delaware: Morphology, cathodoluminescence and backscattered electron zoning, and SHRIMP U-Pb geochronology of zircon and monazite. *Geological Society of America Bulletin*, *118*(1–2), 39–64. https://doi.org/10.1130/b25659.1

Alexeiev, D. V., Biske, Y. S., Wang, B., Djenchuraeva, A. V., Getman, O. F., Aristov, V. A., et al. (2015). Tectono-stratigraphic framework and Palaeozoic evolution of the Chinese South Tianshan. *Geotectonics*, *49*(2), 93–122. https://doi.org/10.1134/s0016852115020028

Allen, M. B., Windley, B. F., & Zhang, C. (1993). Palaeozoic collisional tectonics and magmatism of the Chinese Tien Shan, central Asia. *Tectonophysics*, *220*(1–4), 89–115. https://doi.org/10.1016/0040-1951(93)90225-9

Bachmann, O., Schoene, B., Schnyder, C., & Spikings, R. (2010). The40Ar/39Ar and U/Pb dating of young rhyolites in the Kos-Nisyros volcanic complex, Eastern Aegean Arc, Greece: Age discordance due to excess40Ar in biotite. *Geochemistry, Geophysics, Geosystems*, *11*(8). https://doi.org/10.1029/2010gc003073

Bai, X. J., Qiu, H. N., Liu, W. G., & Mei, L. F. (2018). Automatic $^{40}Ar/^{39}Ar$ dating techniques using multicollector ARGUS VI Noble gas mass spectrometer with self-made peripheral apparatus. *Journal of Earth Sciences*, *29*(2), 408–415. https://doi.org/10.1007/s12583-017-0948-9

Beaumont, C., Nguyen, M. H., Jamieson, R. A., Ellis, S., Law, R. D., Searle, M. P., et al. (2006). *Crustal flow modes in large hot orogens* (Vol. 268). Geological Society of London.

BGMRX. (1993). *Bureau of geology and Mineral Resources of Xinjiang Autonomous Region, Regional Geology of Xinjiang Autonomous Region*. Geological Publishing House.

Biske, Y. S., Alexeiev, D. V., Wang, B., Wang, F., Getman, O. F., Jenchuraeva, A. V., et al. (2012). Structures of the late Palaeozoic thrust belt in the Chinese South Tian Shan. *Doklady Earth Sciences*, *442*(1), 8–12. https://doi.org/10.1134/s1028334x12010060

Brown, M., Cawood, P. A., & Kröner, A. (2009). Metamorphic patterns in orogenic systems and the geological record. In *Earth accretionary systems in space and time* (Vol. 318). Geological Society of London.

Brown, M., & Johnson, T. (2018). Secular change in metamorphism and the onset of global plate tectonics. *American Mineralogist*, *103*(2), 181–196. https://doi.org/10.2138/am-2018-6166

Cai, Z. H., Xu, Z. Q., He, B. Z., & Wang, R. R. (2012). Age and tectonic evolution of ductile shear zones in the eastern Tianshan-Beishan orogenic belt. *Acta Petrologica Sinica*, *28*(6), 1875–1895.

Cai, Z. H., Xu, Z. Q., Tang, Z. M., He, B. Z., & Chen, F. Y. (2011). The crustal deformation during the Early Paleozoic period and the timing of orogeny in Kuruktag area on the northeast margin of Tarim Basin. *Geology in China*, *38*(4), 855–867.

Cao, Y. C., Wang, B., Jahn, B. M., Cluzel, D., Shu, L. S., & Zhong, L. L. (2017). Late Paleozoic arc magmatism in the southern Yili Block (NW China): Insights to the geodynamic evolution of the Balkhash—Yili continental margin, Central Asian Orogenic Belt. *Lithos*, *278–281*, 111–125. https://doi.org/10.1016/j.lithos.2017.01.023

Carroll, A. R., Graham, S. A., Hendrix, M. S., Ying, D., & Zhou, D. (1995). Late Paleozoic tectonic amalgamation of northwestern China - Sedimentary record of the Northern Tarim, Northwestern Turpan, and Southern Junggar Basins. *Geological Society of America Bulletin*, *107*(5), 571–594. https://doi.org/10.1130/0016-7606(1995)107<0571:Lptaon>2.3.Co;2

Charvet, J., Shu, L. S., & Laurent-Charvet, S. (2007). Paleozoic structural and geodynamic evolution of eastern Tianshan (NW China): Welding of the Tarim and Junggar plates. *Episodes*, *30*(3), 162–186. https://doi.org/10.1007/s00254-007-0834-3

Charvet, J., Shu, L. S., Laurent-Charvet, S., Wang, B., Faure, M., Cluzel, D., et al. (2011). Palaeozoic tectonic evolution of the Tianshan belt, NW China. *Science China Earth Sciences*, *54*(2), 166–184. https://doi.org/10.1007/s11430-010-4138-1

Chen, B., Long, X. P., Yuan, C., Wang, Y. J., Sun, M., Xiao, W. J., et al. (2015). Geochronology and geochemistry of late Ordovician–early Devonian gneissic granites in the Kumishi area, northern margin of the South Tianshan belt: Constraints on subduction process of the South Tianshan Ocean. *Journal of Asian Earth Sciences*, *113*, 293–309. https://doi.org/10.1016/j.jseaes.2014.09.034

Chen, C. M., Lu, H. F., Jia, D., Cai, D. S., & Wu, S. M. (1999). Closing history of the southern Tianshan oceanic basin, western China: An oblique collisional orogeny. *Tectonophysics*, *302*(1–2), 23–40. https://doi.org/10.1016/S0040-1951(98)00273-X

Chen, G. W., Yang, J. X., Liu, R., & Yang, G. (2019). Potassic alkaline granitoid magmatism in the northern margin of the Tarim Craton: First evidence of a back-arc extensional environment. *Geological Journal*, *55*(1), 771–785. https://doi.org/10.1002/gj.3450

Chen, Y. B., Zhang, G. W., Liu, X. M., Xiong, X. L., Yuan, C., & Chen, L. L. (2012). Zircons LA-ICP-MS U-Pb dating on the Baluntai deformed granitoids, Central Tianshan Block, Northwest China, and its tectonic implications. *Geological Review*, *58*(1), 117–125. https://doi.org/10.16509/j.georeview.2012.01.020

Clay, P. L., Kelley, S. P., Sherlock, S. C., & Barry, T. L. (2011). Partitioning of excess argon between alkali feldspars and glass in a young volcanic system. *Chemical Geology*, *289*(1–2), 12–30. https://doi.org/10.1016/j.chemgeo.2011.07.005

Collins, W. J. (2002a). Hot orogens, tectonic switching, and creation of continental crust. *Geology*, *30*(6), 535–538. https://doi.org/10.1130/0091-7613(2002)030

Collins, W. J. (2002b). Nature of extensional accretionary orogens. *Tectonics*, *21*(4), 6-1–6-12. https://doi.org/10.1029/2000tc001272

Cosgrove, J. W. (1997). The influence of mechanical anisotropy on the behaviour of the lower crust. *Tectonophysics*, *280*(1–2), 1–14. https://doi.org/10.1016/s0040-1951(97)00145-5

Cui, J. W., Tian, L. M., Sun, J. Y., Yang, C., & Li, S. (2018). Geochronology and geochemistry of early Palaeozoic intrusive rocks in the Lajishan area of the eastern south Qilian Belt, Tibetan Plateau: Implications for the tectonic evolution of South Qilian. *Geological Journal*, *54*(6), 3404–3420. https://doi.org/10.1002/gj.3327

Currie, C. A., Huismans, R. S., & Beaumont, C. (2008). Thinning of continental backarc lithosphere by flow-induced gravitational instability. *Earth and Planetary Science Letters*, *269*(3–4), 436–447. https://doi.org/10.1016/j.epsl.2008.02.037

Díaz-Azpiroz, M., Barcos, L., Balanyá, J. C., Fernández, C., Expósito, I., & Czeck, D. M. (2014). Applying a general triclinic transpression model to highly partitioned brittle-ductile shear zones: A case study from the Torcal de Antequera massif, external Betics, southern Spain. *Journal of Structural Geology*, *68*, 316–336. https://doi.org/10.1016/j.jsg.2014.05.010

Domeier, M. (2018). Early Paleozoic tectonics of Asia: Towards a full-plate model. *Geoscience Frontiers*, *9*(3), 789–862. https://doi.org/10.1016/j.gsf.2017.11.012

Dong, Y. P., Zhang, G. X., Neubauer, F., Liu, X. M., Hauzenberger, C., Zhou, D. W., & Li, W. (2011). Syn- and post-collisional granitoids in the Central Tianshan orogen: Geochemistry, geochronology and implications for tectonic evolution. *Gondwana Research*, *20*(2–3), 568–581. https://doi.org/10.1016/j.gr.2011.01.013

Dong, Y. P., Zhou, D. W., Zhang, G. W., Zhang, C. L., Xia, L. Q., Xu, X. Y., et al. (2005). Tectonic setting of the Wuwamen ophiolite at the southern margin of Middle Tianshan Belt. *Acta Petrologica Sinica*, *21*(1), 37–44.

Dong, Y. P., Zhou, D. W., Zhang, G. W., Zhao, X., Luo, J. H., & Xu, J. G. (2006). Geology and geochemistry of the Gangou ophiolitic melange at the northern margin of the Middle Tianshan Belt. *Acta Petrologica Sinica*, *22*(1), 49–56.

Ducea, M. N., Kidder, S., & Zandt, G. (2003). Arc composition at mid-crustal depths: Insights from the Coast Ridge Belt, Santa Lucia Mountains, California. *Geophysical Research Letters*, *30*(13). https://doi.org/10.1029/2002gl016297

Faber, C., Stünitz, H., Gasser, D., Jeřábek, P., Kraus, K., Corfu, F., et al. (2019). Anticlockwise metamorphic pressure–temperature paths and nappe stacking in the Reisa Nappe Complex in the Scandinavian Caledonides, northern Norway: Evidence for weakening of lower continental crust before and during continental collision. *Solid Earth*, *10*(1), 117–148. https://doi.org/10.5194/se-10-117-2019

Foster, D. A., & Gray, D. R. (2000). Evolution and structure of the Lachlan Fold Belt (Orogen) of Eastern Australia. *Annual Review of Earth and Planetary Sciences*, *28*(1), 47–80. https://doi.org/10.1146/annurev.earth.28.1.47

Fu, D., Kusky, T., Wilde, S. A., Polat, A., Huang, B., & Zhou, Z. P. (2018). Early Paleozoic collision-related magmatism in the eastern North Qilian orogen, northern Tibet: A linkage between accretionary and collisional orogenesis. *GSA Bulletin*, *131*(5–6), 1031–1056. https://doi.org/10.1130/b35009.1

Gao, J., He, G. Q., Li, M. S., Xiao, X. C., Tang, Y. Q., Wang, J., & Zhao, M. (1995). The mineralogy, petrology, metamorphic ptdt Trajectory and exhumation mechanism of Blueschists, South Tianshan, northwestern China. *Tectonophysics*, *250*(1–3), 151–168. https://doi.org/10.1016/0040-1951(95)00026-6

Gao, J., Li, M. S., Xiao, X. C., Tang, Y. Q., & He, G. Q. (1998). Paleozoic tectonic evolution of the Tianshan Orogen, northwestern China. *Tectonophysics*, *287*(1–4), 213–231. https://doi.org/10.1016/S0040-1951(97)00211-4

Gao, J., Qian, Q., Long, L. L., Zhang, X., Li, J. L., & Su, W. (2009). Accretionary orogenic process of Western Tianshan, China. *Geological Bulletin of China*, *28*(12), 1804–1816.

Gao, J., Zhang, L. F., & Liu, S. W. (2000). The $^{40}Ar/^{39}Ar$ age record of formation and uplift of the blueschists and eclogites in the western Tianshan Mountains. *Chinese Science Bulletin*, *45*(11), 1047–1052. https://doi.org/10.1007/bf02884989

Gao, R., Xiao, L., Wang, H. Q., Wang, G. C., Luo, Y. J., & Liu, H. (2012). Geochemical characteristics and LA-ICP-MS U-Pb zircon ages of volcanic rocks in Kaidu River,South Tianshan,Xinjiang,and their geological significance. *Acta Petrologica et Mineralogica*, *31*(4), 541–553.

Gao, Z. J., Chen, J. B., Lu, S. N., Peng, C. W., & Qin, Z. Y. (1993). *The Precambrian geology in northern Xinjiang (Precambrian geology no. 6)*. Geological Publishing House.

Ge, R., Wilde, S. A., Zhu, W., Zhou, T., & Si, Y. (2022). Formation and evolution of Archean continental crust: A thermodynamic – Geochemical perspective of granitoids from the Tarim craton, NW China. *Earth-Science Reviews*, *234*, 104219. https://doi.org/10.1016/j.earscirev.2022.104219

Ge, R. F., Wilde, S. A., Kemp, A. I. S., Jeon, H., Martin, L. A. J., Zhu, W. B., & Wu, H. (2020). Generation of Eoarchean continental crust from altered mafic rocks derived from a chondritic mantle: The ~3.72 Ga Aktash gneisses, Tarim Craton (NW China). *Earth and Planetary Science Letters*, *538*, 116225. https://doi.org/10.1016/j.epsl.2020.116225

Ge, R. F., Zhu, W. B., & Wilde, S. A. (2016). Mid-Neoproterozoic (ca. 830-800 Ma) metamorphic P-Tpaths link Tarim to the circum-Rodinia subduction-accretion system. *Tectonics*, *35*(6), 1465–1488. https://doi.org/10.1002/2016tc004177

Ge, R. F., Zhu, W. B., Wilde, S. A., & He, J. W. (2014a). Zircon U–Pb–Lu–Hf–O isotopic evidence for ≥3.5Ga crustal growth, reworking and differentiation in the northern Tarim Craton. *Precambrian Research*, *249*, 115–128. https://doi.org/10.1016/j.precamres.2014.05.004

Ge, R. F., Zhu, W. B., Wilde, S. A., He, J. W., Cui, X., Wang, X., & Bihai, Z. (2014b). Neoproterozoic to Paleozoic long-lived accretionary orogeny in the northern Tarim Craton. *Tectonics*, *33*(3), 302–329. https://doi.org/10.1002/2013tc003501

Ge, R. F., Zhu, W. B., Wilde, S. A., & Wu, H. L. (2018). Remnants of Eoarchean continental crust derived from a subducted proto-arc. *Science Advances*, *4*(2), eaao3159. https://doi.org/10.1126/sciadv.aao3159

Ge, R. F., Zhu, W. B., Wu, H. L., He, J. W., & Zheng, B. H. (2013). Zircon U–Pb ages and Lu–Hf isotopes of Paleoproterozoic metasedimentary rocks in the Korla Complex, NW China: Implications for metamorphic zircon formation and geological evolution of the Tarim Craton. *Precambrian Research*, *231*, 1–18. https://doi.org/10.1016/j.precamres.2013.03.003

Ge, R. F., Zhu, W. B., Wu, H. L., Zheng, B. H., Zhu, X. Q., & He, J. W. (2012a). The paleozoic northern margin of the Tarim craton: Passive or active? *Lithos*, *142*, 1–15. https://doi.org/10.1016/j.lithos.2012.02.010

Ge, R. F., Zhu, W. B., Zheng, B. H., Wu, H. L., He, J. W., & Zhu, X. Q. (2012b). Early Pan-African magmatism in the Tarim Craton: Insights from zircon U–Pb–Lu–Hf isotope and geochemistry of granitoids in the Korla area, NW China. *Precambrian Research*, *212–213*, 117–138. https://doi.org/10.1016/j.precamres.2012.05.001

Glen, R. A. (2013). Refining accretionary orogen models for the Tasmanides of eastern Australia. *Australian Journal of Earth Sciences*, *60*(3), 315–370. https://doi.org/10.1080/08120099.2013.772537

Grimes, C. B., John, B. E., Cheadle, M. J., Mazdab, F. K., Wooden, J. L., Swapp, S., & Schwartz, J. J. (2009). On the occurrence, trace element geochemistry, and crystallization history of zircon from in situ ocean lithosphere. *Contributions to Mineralogy and Petrology*, *158*(6), 757–783. https://doi.org/10.1007/s00410-009-0409-2

Grove, M., & Harrison, T. M. (1996). $^{40}Ar^*$ diffusion in Fe-rich biotite. *American Mineralogist*, *81*(7–8), 940–951. https://doi.org/10.2138/am-1996-7-816

Guo, R. Q., Liang, W. B., Liu, G. P., Zou, M. Y., Hu, X. Y., Wu, H. N., et al. (2020). Chronology, geochemical characteristics and geological significance of Early Devonian olivine gabbro in the Kuruktagxi section of Xinjiang. *Chinese Journal of Geology*, *55*(1), 234–253.

Guo, R. Q., Nijiati, A., Qin, Q., Jia, X. L., Zhu, Z. X., Wang, K. Z., et al. (2013). Geological characteristics and tectonic significance of Silurian granitic intrusions in the northern Tarim craton,Xinjiang. *Geological Bulletin of China*, *32*(2/3), 220–238.

Guo, Y., Zhao, G., Guo, R., Han, Y., Wei, Z., Zhou, N., & Ju, P. (2022). Late Paleoproterozoic orogenic evolution of the northern Tarim Craton, NW China: Insights from phase equilibrium modeling and zircon U-Pb geochronology of metapelitic granulite in the Kuluketage area. *Gondwana Research*, *106*, 351–366. https://doi.org/10.1016/j.gr.2022.02.005

Han, B. F., Guo, Z. J., Zhang, Z. C., Zhang, L., Chen, J. F., & Song, B. (2010). Age, geochemistry, and tectonic implications of a late Paleozoic stitching pluton in the North Tian Shan suture zone, western China. *Geological Society of America Bulletin*, *122*(3–4), 627–640. https://doi.org/10.1130/b26491.1

Han, Y. G., & Zhao, G. C. (2018). Final amalgamation of the Tianshan and Junggar orogenic collage in the southwestern Central Asian Orogenic Belt: Constraints on the closure of the Paleo-Asian Ocean. *Earth-Science Reviews*, *186*, 129–152. https://doi.org/10.1016/j.earscirev.2017.09.012

Han, Y. G., Zhao, G. C., Cawood, P. A., Sun, M., Eizenhofer, P. R., Hou, W. Z., et al. (2016). Tarim and North China cratons linked to northern Gondwana through switching accretionary tectonics and collisional orogenesis. *Geology*, *44*(2), 95–98. https://doi.org/10.1130/G37399.1

Han, Y. G., Zhao, G. C., Sun, M., Eizenhöfer, P. R., Hou, W. Z., Zhang, X. R., et al. (2015). Paleozoic accretionary orogenesis in the Paleo-Asian Ocean: Insights from detrital zircons from Silurian to Carboniferous strata at the northwestern margin of the Tarim Craton. *Tectonics*, *34*(2), 334–351. https://doi.org/10.1002/2014tc003668

Harris, L. B. (2003). Folding in high-grade rocks due to back-rotation between shear zones. *Journal of Structural Geology*, *25*(2), 223–240. https://doi.org/10.1016/s0191-8141(02)00024-x

Hu, A. Q., Jahn, B. M., Zhang, G. X., Chen, Y. B., & Zhang, Q. F. (2000). Crustal evolution and phanerozoic crustal growth in northern Xinjiang: Nd isotopic evidence. Part I. Isotopic characterization of basement rocks. *Tectonophysics*, *328*(1–2), 15–51. https://doi.org/10.1016/S0040-1951(00)00176-1

Hu, A. Q., Wei, G. J., Zhang, J. B., Deng, W. F., & Chen, L. L. (2007). SHRIMP U-Pb age for zircons of East Tianhu granitic gneiss and tectoic evolution significance from the eastern Tianshan Mountains, Xinjiang, China. *Acta Petrologica Sinica*, *23*(8), 1795–1802.

Hu, Z., Zhang, W., Liu, Y., Gao, S., Li, M., Zong, K., et al. (2015). Wave" signal-smoothing and mercury-removing device for laser ablation quadrupole and multiple collector ICPMS analysis: Application to lead isotope analysis. *Analytical Chemistry*, *87*(2), 1152–1157. https://doi.org/10.1021/ac503749k

Huang, H., Wang, T., Qin, Q., Hou, J. Y., Tong, Y., Guo, L., et al. (2015a). Zircon Hf isotopic characteristics of granitoids from the Baluntai Region, Central Tianshan: Implications for tectonic evolution and continental growth. *Acta Geologica Sinica*, *89*(12), 2286–2313.

Huang, H., Wang, T., Tong, Y., Qin, Q., Ma, X. X., & Yin, J. Y. (2020). Rejuvenation of ancient micro-continents during accretionary orogenesis: Insights from the Yili Block and adjacent regions of the SW Central Asian Orogenic Belt. *Earth-Science Reviews*, *208*, 103255. https://doi.org/10.1016/j.earscirev.2020.103255

Huang, H., Zhang, Z. C., Santosh, M., Cheng, Z. G., Wang, T., & Liu, Y. (2018). Crustal evolution in the South Tianshan terrane: Constraints from detrital zircon geochronology and implications for continental growth in the Central Asian Orogenic Belt. *Geological Journal*, *54*(3), 1379–1400. https://doi.org/10.1002/gj.3235

Huang, H., Zhang, Z. C., Santosh, M., & Zhang, D. Y. (2014). Geochronology, geochemistry and metallogenic implications of the Boziguo'er rare metal-bearing peralkaline granitic intrusion in South Tianshan, NW China. *Ore Geology Reviews*, *61*, 157–174. https://doi.org/10.1016/j.oregeorev.2014.01.011

Huang, H., Zhang, Z. C., Santosh, M., Zhang, D. Y., Zhao, Z. D., & Liu, J. L. (2013a). Early paleozoic tectonic evolution of the South Tianshan Collisional Belt: Evidence from geochemistry and zircon U-Pb geochronology of the Tie'reke monzonite Pluton, Northwest China. *The Journal of Geology*, *121*(4), 401–424. https://doi.org/10.1086/670653

Huang, Z. Y., Long, X. P., Kröner, A., Yuan, C., Wang, Q., Sun, M., et al. (2013b). Geochemistry, zircon U–Pb ages and Lu–Hf isotopes of early Paleozoic plutons in the northwestern Chinese Tianshan: Petrogenesis and geological implications. *Lithos*, *182–183*, 48–66. https://doi.org/10.1016/j.lithos.2013.09.009

Huang, Z. Y., Long, X. P., Kröner, A., Yuan, C., Wang, Y. J., Chen, B., & Zhang, Y. (2015b). Neoproterozoic granitic gneisses in the Chinese Central Tianshan Block: Implications for tectonic affinity and Precambrian crustal evolution. *Precambrian Research*, *269*, 73–89. https://doi.org/10.1016/j.precamres.2015.08.005

Huang, Z. Y., Long, X. P., Wang, X. C., Zhang, Y. Y., Du, L., Yuan, C., & Xiao, W. (2017). Precambrian evolution of the Chinese Central Tianshan Block: Constraints on its tectonic affinity to the Tarim Craton and responses to supercontinental cycles. *Precambrian Research*, *295*, 24–37. https://doi.org/10.1016/j.precamres.2017.04.014

Huang, Z. Y., Long, X. P., Yuan, C., Sun, M., Wang, Y. J., Zhang, Y. Y., & Chen, B. (2016). Detrital zircons from Neoproterozoic sedimentary rocks in the Yili Block: Constraints on the affinity of microcontinents in the southern Central Asian Orogenic Belt. *Gondwana Research*, *37*, 39–52. https://doi.org/10.1016/j.gr.2016.05.009

Hyndman, R. D. (2019). Mountain building orogeny in precollision hot backarcs: North American Cordillera, India-Tibet, and Grenville Province. *Journal of Geophysical Research: Solid Earth*, *124*(2), 2057–2079. https://doi.org/10.1029/2018jb016697

Hyndman, R. D., Currie, C. A., & Mazzotti, S. P. (2005). Subduction zone backarcs, mobile belts, and orogenic heat. *Geological Society of America Today*, *15*(2), 4. https://doi.org/10.1130/1052-5173(2005)015

Hyndman, R. D., & Lewis, T. J. (1995). Review: The thermal regime along the southern Canadian Cordillera Lithoprobe corridor. *Canadian Journal of Earth Sciences*, *32*(10), 1611–1617. https://doi.org/10.1139/e95-129

Jackson, S. E., Pearson, N. J., Griffin, W. L., & Belousova, E. A. (2004). The application of laser ablation-inductively coupled plasma-mass spectrometry to in situ U-Pb zircon geochronology. *Chemical Geology*, *211*(1–2), 47–69. https://doi.org/10.1016/j.chemgeo.2004.06.017

Jahn, B. M. (2004). The Central Asian Orogenic Belt and growth of the continental crust in the phanerozoic. *Geological Society, London, Special Publications*, *226*(1), 73–100. https://doi.org/10.1144/gsl.Sp.2004.226.01.05

Jamieson, R. A., Beaumont, C., Nguyen, M. H., & Lee, B. (2002). Interaction of metamorphism, deformation and exhumation in large convergent orogens. *Journal of Metamorphic Geology*, *20*(1), 9–24. https://doi.org/10.1046/j.0263-4929.2001.00357.x

Jeřábek, P., Lexa, O., Schulmann, K., & Plašienka, D. (2012). Inverse ductile thinning via lower crustal flow and fold-induced doming in the West Carpathian Eo-Alpine collisional wedge. *Tectonics*, *31*(5). https://doi.org/10.1029/2012tc003097

Jiang, T., Gao, J., Klemd, R., Qian, Q., Zhang, X., Xiong, X. M., et al. (2014). Paleozoic ophiolitic mélanges from the South Tianshan Orogen, NW China: Geological, geochemical and geochronological implications for the geodynamic setting. *Tectonophysics*, *612–613*, 106–127. https://doi.org/10.1016/j.tecto.2013.11.038

Kong, W. L., Zhang, Z. C., Huang, H., Cheng, Z. G., & Santosh, M. (2019). Geochemistry and zircon U–Pb geochronology of the oxidaban intrusive complex: Implication for Paleozoic tectonic evolution of the South Tianshan Orogenic Belt, China. *Lithos*, *324–325*, 265–279. https://doi.org/10.1016/j.lithos.2018.11.013

Koppers, A. A. P. (2002). ArArCALC—Software for 40Ar/39Ar age calculations. *Computers and Geosciences*, *28*(5), 605–619. https://doi.org/10.1016/s0098-3004(01)00095-4

Kruckenberg, S. C., Vanderhaeghe, O., Ferré, E. C., Teyssier, C., & Whitney, D. L. (2011). Flow of partially molten crust and the internal dynamics of a migmatite dome, Naxos, Greece. *Tectonics*, *30*(3). https://doi.org/10.1029/2010tc002751

Laurent-Charvet, S., Charvet, J., Shu, L. S., Ma, R. S., & Lu, H. F. (2002). Palaeozoic late collisional strike-slip deformations in Tianshan and Altay, Eastern Xinjiang, NW China. *Terra Nova*, *14*(4), 249–256. https://doi.org/10.1046/j.1365-3121.2002.00417.x

Lee, K. Y. (1985). *Geology of the Tarim Basin with special emphasis on petroleum deposits, Xinjiang Uygur Zizhiqu, Northwest China* (Vol. 55PP). U.S. Geological Survey, Open File Report.

Lei, R. X., Wu, C. Z., Chi, G. X., Chen, G., Gu, L. X., & Jiang, Y. X. (2012). Petrogenesis of the palaeoproterozoic Xishankou pluton, northern Tarim block, northwest China: Implications for assembly of the supercontinent Columbia. *International Geology Review*, *54*(15), 1829–1842. https://doi.org/10.1080/00206814.2012.678045

Li, C., Xiao, W. J., Han, C. M., Zhou, K. F., Zhang, J. E., & Zhang, Z. X. (2014a). Late Devonian–early Permian accretionary orogenesis along the North Tianshan in the southern Central Asian Orogenic Belt. *International Geology Review*, *57*(5–8), 1023–1050. https://doi.org/10.1080/00206814.2014.913268

Li, J. L., Su, W., Zhang, X., & Liu, X. (2009). Zircon Cameca U-Pb dating and its significance for granulite-facies gneisses from the western Awulale Mountain, West Tianshan, China. *Geological Bulletin of China*, *28*(12), 1852–1862.

Li, P. F., Jiang, Y. D., Xia, X. P., Jourdan, F., Yuan, C., Cai, K. D., et al. (2020). Tectonic evolution of the Chinese Tianshan Orogen from subduction to arc-continent collision: Insight from polyphase deformation along the Gangou section, Central Asia. *GSA Bulletin*, *132*(11–12), 2529–2552. https://doi.org/10.1130/b35353.1

Li, S. Z., Zhao, S. J., Liu, X., Cao, H. H., Yu, S., Li, X. Y., et al. (2018). Closure of the proto-Tethys Ocean and early Paleozoic amalgamation of microcontinental blocks in East Asia. *Earth-Science Reviews*, *186*, 37–75. https://doi.org/10.1016/j.earscirev.2017.01.011

Li, Y. J., Sun, L. D., Yang, H. J., Zhang, G. Y., Zeng, C. M., Feng, X. J., et al. (2014b). New discovery of Late Silurian-Carboniferous extensional structure in Tarim Basin and its geological significance. *Chinese Journal of Geology*, *49*(1), 30–48. https://doi.org/10.3969/j.issn.0563-5020.2014.01.003

Li, Y. J., Wen, L., Yang, H. J., Zhang, G. Y., Shi, J., Peng, G. X., et al. (2015). New discovery and geological significance of late silurian–Carboniferous extensional structures in Tarim Basin. *Journal of Asian Earth Sciences*, *98*, 304–319. https://doi.org/10.1016/j.jseaes.2014.11.020

Liang, W. B., Guo, R. Q., Liu, G. P., Zou, M. Y., Hu, X. Y., Wu, H. N., et al. (2019). LA-ICP-MS zircon U-Pb age and geochemistry of the Olivine Gabbro Dike in the Western Segment of Kuruktag, Xinjiang and its tectonic significance. *Geological Science and Technology Information*, *38*(1), 58–67. https://doi.org/10.19509/j.cnki.dzkq.2019.0107

Lin, W., Chu, Y., Ji, W. B., Zhang, Z. B., Shi, Y. H., Wang, Z. Y., et al. (2013). Geochronological and geochemical constraints for a middle Paleozoic continental arc on the northern margin of the Tarim block: Implications for the Paleozoic tectonic evolution of the South Chinese Tianshan. *Lithosphere*, *5*(4), 355–381. https://doi.org/10.1130/l231.1

Lin, W., Faure, M., Shi, Y. H., Wang, Q. C., & Li, Z. (2009). Palaeozoic tectonics of the south-western Chinese Tianshan: New insights from a structural study of the high-pressure/low-temperature metamorphic belt. *International Journal of Earth Sciences*, *98*(6), 1259–1274. https://doi.org/10.1007/s00531-008-0371-7

Liou, J. G., Graham, S. A., Maruyama, S., Wang, X., Xiao, X., Carroll, A. R., et al. (1989). Proterozoic blueschist belt in western China: Best documented Precambrian blueschists in the world. *Geology*, *17*(12), 1127. https://doi.org/10.1130/0091-7613(1989)017

Liu, G. P., Guo, R. Q., Wei, Z., Sun, M. J., Cui, T., Wu, H. N., et al. (2021). Geochemical characteristics and significance of the whole rock Sr-Nd and zircon Hf isotopic in the paleozoic granite-plutons in Kuruktag, Xinjiang. *Northwestern Geology*, *54*(3), 39–50.

Liu, J. S., Wang, B., Ni, X. H., Song, F., Sun, Z. C., Deng, J., et al. (2022). Late Devonian transition from advancing to retreating subduction in the SW Central Asian Orogenic Belt: Insights from multiple deformation and magmatic events in the southern Yili Block, NW China. *Gondwana Research*, *105*, 468–487. https://doi.org/10.1016/j.gr.2021.10.001

Liu, K., Zhang, J. J., Xiao, W. J., Wilde, S. A., & Alexandrov, I. (2020). A review of magmatism and deformation history along the NE Asian margin from ca. 95 to 30 Ma: Transition from the Izanagi to Pacific plate subduction in the early Cenozoic. *Earth-Science Reviews*, *209*, 103317. https://doi.org/10.1016/j.earscirev.2020.103317

Liu, Y. S., Gao, S., Kelemen, P. B., & Xu, W. L. (2008). Recycled crust controls contrasting source compositions of Mesozoic and Cenozoic basalts in the North China Craton. *Geochimica et Cosmochimica Acta*, *72*(9), 2349–2376. https://doi.org/10.1016/j.gca.2008.02.018

Long, L. L., Gao, J., Wang, J. B., Qian, Q., Xiong, X. M., Wang, Y. W., et al. (2010a). Geochemistry and SHRIMP zircon U-Pb age of post-collisional granites in the Southwest Tianshan Orogenic Belt of China: Examples from the Heiyingshan and Laohutai plutons. *Acta Geologica Sinica - English Edition*, *82*(2), 415–424. https://doi.org/10.1111/j.1755-6724.2008.tb00592.x

Long, X. P., Sun, M., Yuan, C., Kröner, A., & Hu, A. Q. (2012). Zircon REE patterns and geochemical characteristics of Paleoproterozoic anatectic granite in the northern Tarim Craton, NW China: Implications for the reconstruction of the Columbia supercontinent. *Precambrian Research*, *222–223*, 474–487. https://doi.org/10.1016/j.precamres.2011.09.009

Long, X. P., Yuan, C., Sun, M., Kroner, A., Zhao, G. C., Wilde, S., & Hu, A. (2011a). Reworking of the Tarim Craton by underplating of mantle plume-derived magmas: Evidence from Neoproterozoic granitoids in the Kuluketage area, NW China. *Precambrian Research*, *187*(1–2), 1–14. https://doi.org/10.1016/j.precamres.2011.02.001

Long, X. P., Yuan, C., Sun, M., Zhao, G. C., Xiao, W. J., Wang, Y. J., et al. (2010b). Archean crustal evolution of the northern Tarim craton, NW China: Zircon U–Pb and Hf isotopic constraints. *Precambrian Research*, *180*(3–4), 272–284. https://doi.org/10.1016/j.precamres.2010.05.001

Long, X. P., Yuan, C. O., Sun, M., Xiao, W. J., Zhao, G. C., Zhou, K. F., et al. (2011b). The discovery of the oldest rocks in the Kuluketage area and its geological implications. *Science China Earth Sciences*, *54*(3), 342–348. https://doi.org/10.1007/s11430-010-4156-z

Lu, S. N., Li, H. K., Zhang, C. L., & Niu, G. H. (2008). Geological and geochronological evidence for the Precambrian evolution of the Tarim Craton and surrounding continental fragments. *Precambrian Research*, *160*(1–2), 94–107. https://doi.org/10.1016/j.precamres.2007.04.025

Lü, Z., & Zhang, L. F. (2012). Coesite in the eclogite and schist of the Atantayi Valley, southwestern Tianshan, China. *Chinese Science Bulletin*, *57*(13), 1467–1472. https://doi.org/10.1007/s11434-012-4979-4

Ludwig, K. R. (2003). *Isoplot/ex, a geochronological toolkit for Microsoft Excel, version 3.00*. Berkeley Geochronology Center.

Ma, X. X., Shu, L. S., Jahn, B. M., Zhu, W. B., & Faure, M. (2012a). Precambrian tectonic evolution of Central Tianshan, NW China: Constraints from U–Pb dating and in situ Hf isotopic analysis of detrital zircons. *Precambrian Research*, *222–223*, 450–473. https://doi.org/10.1016/j.precamres.2011.06.004

Ma, X. X., Shu, L. S., Meert, J. G., & Li, J. Y. (2014). The Paleozoic evolution of Central Tianshan: Geochemical and geochronological evidence. *Gondwana Research*, *25*(2), 797–819. https://doi.org/10.1016/j.gr.2013.05.015

Ma, X. X., Shu, L. S., Santosh, M., & Li, J. Y. (2012b). Detrital zircon U–Pb geochronology and Hf isotope data from Central Tianshan suggesting a link with the Tarim Block: Implications on Proterozoic supercontinent history. *Precambrian Research*, *206–207*, 1–16. https://doi.org/10.1016/j.precamres.2012.02.015

Ma, X. X., Shu, L. S., Santosh, M., & Li, J. Y. (2012c). Petrogenesis and tectonic significance of an early Palaeozoic mafic-intermediate suite of rocks from the Central Tianshan, northwest China. *International Geology Review*, *55*(5), 548–573. https://doi.org/10.1080/00206814.2012.727575

Mao, L. J., He, Z. Y., Zhang, Z. M., Klemd, R., Xiang, H., Tian, Z. L., & Zong, K. Q. (2015). Origin and geodynamic significance of the early Mesozoic Weiya LP and HT granulites from the Chinese Eastern Tianshan. *Lithos*, *239*, 142–156. https://doi.org/10.1016/j.lithos.2015.10.016

Mao, Q. G., Xiao, W. J., Fang, T. H., Wang, J. B., Han, C. M., Sun, M., & Yuan, C. (2012). Late Ordovician to early Devonian adakites and Nb-enriched basalts in the Liuyuan area, Beishan, NW China: Implications for early Paleozoic slab-melting and crustal growth in the southern Altaids. *Gondwana Research*, *22*(2), 534–553. https://doi.org/10.1016/j.gr.2011.06.006

McKenzie, D., & Bickle, M. J. (1988). The volume and composition of melt generated by extension of the lithosphere. *Journal of Petrology*, *29*(3), 625–679. https://doi.org/10.1093/petrology/29.3.625

Merdith, A. S., Williams, S. E., Collins, A. S., Tetley, M. G., Mulder, J. A., Blades, M. L., et al. (2021). Extending full-plate tectonic models into deep time: Linking the Neoproterozoic and the Phanerozoic. *Earth-Science Reviews*, *214*, 103477. https://doi.org/10.1016/j.earscirev.2020.103477

Metcalfe, I. (1994). Gondwanaland origin, dispersion, and accretion of East and Southeast Asian continental terranes. *Journal of South American Earth Sciences*, *7*(3–4), 333–347. https://doi.org/10.1016/0895-9811(94)90019-1

Metcalfe, I. (1996). Gondwanaland dispersion, Asian accretion and evolution of eastern Tethys. *Australian Journal of Earth Sciences*, *43*(6), 605–623. https://doi.org/10.1080/08120099608728282

Metcalfe, I. (2013). Gondwana dispersion and Asian accretion: Tectonic and palaeogeographic evolution of eastern Tethys. *Journal of Asian Earth Sciences*, *66*, 1–33. https://doi.org/10.1016/j.jseaes.2012.12.020

Morrissey, L. J., Hand, M., Raimondo, T., & Kelsey, D. E. (2014). Long-lived high-T, low-P granulite facies metamorphism in the Arunta Region, central Australia. *Journal of Metamorphic Geology*, *32*(1), 25–47. https://doi.org/10.1111/jmg.12056

Mühlberg, M., Hegner, E., Klemd, R., Pfänder, J. A., Kaliwoda, M., & Biske, Y. S. (2016). Late Carboniferous high-pressure metamorphism of the Kassan metamorphic complex (Kyrgyz Tianshan) and assembly of the SW central asian orogenic belt. *Lithos*, *264*, 41–55. https://doi.org/10.1016/j.lithos.2016.08.008

Ning, J., & Jiang, Y. D. (2023). Geochronological data of Paleozoic igneous and metamorphic rocks from the NE Tarim Craton and its adjacent regions (version 2) [Dataset]. Mendeley Data. https://doi.org/10.17632/xdhxyk6yvh.2

Pei, F. P., Zhang, Y., Wang, Z. W., Cao, H. H., Xu, W. L., Wang, Z. J., et al. (2016). Early–middle paleozoic subduction–collision history of the south-eastern Central Asian Orogenic Belt: Evidence from igneous and metasedimentary rocks of central Jilin Province, NE China. *Lithos*, *261*, 164–180. https://doi.org/10.1016/j.lithos.2015.12.010

Platt, J. P. (1983). Progressive refolding in ductile shear zones. *Journal of Structural Geology*, *5*(6), 619–622. https://doi.org/10.1016/0191-8141(83)90074-3

Price, N. J., & Cosgrove, J. W. (1990). *Analysis of geological structures*. Cambridge University Press.

Qin, Q., Huang, H., Wang, T., Guo, R. Q., Zhang, Z. C., & Tong, Y. (2016). Relationship of the Tarim Craton to the Central Asian Orogenic Belt: Insights from Devonian intrusions in the northern margin of Tarim Craton, China. *International Geology Review*, *58*(16), 2007–2028. https://doi.org/10.1080/00206814.2016.1199289

Rey, P. F., Teyssier, C., & Whitney, D. L. (2009). Extension rates, crustal melting, and core complex dynamics. *Geology*, *37*(5), 391–394. https://doi.org/10.1130/g25460a.1

Rod, E. (2007). Discussion: Evolution of central eastern Australia during the palaeozoic and early mesozoic. *Journal of the Geological Society of Australia*, *28*(1–2), 95–96. https://doi.org/10.1080/00167618108729146

Rojas, A. Y., Kröner, A., Alexeiev, D. V., Jeffreys, T., Khudoley, A. K., Wong, J., et al. (2014). Detrital and igneous zircon ages for suprac-rustal rocks of the Kyrgyz Tianshan and palaeogeographic implications. *Gondwana Research*, *26*(3–4), 957–974. https://doi.org/10.1016/j.gr.2013.09.005

Rong, J. Y., Boucot, A. J., Su, Y. Z., & Strusz, D. L. (1995). Biogeographical analysis of Late Silurian Brachiopod Faunas, Chiefly from Asia and Australia. *Lethaia*, *28*(1), 39–60. https://doi.org/10.1111/j.1502-3931.1995.tb01592.x

Rosenberg, C. L., & Handy, M. R. (2005). Experimental deformation of partially melted granite revisited: Implications for the continental crust. *Journal of Metamorphic Geology*, *23*(1), 19–28. https://doi.org/10.1111/j.1525-1314.2005.00555.x

Sarkarinejad, K., Faghih, A., & Grasemann, B. (2008). Transpressional deformations within the Sanandaj–Sirjan metamorphic belt (Zagros Mountains, Iran). *Journal of Structural Geology*, *30*(7), 818–826. https://doi.org/10.1016/j.jsg.2008.03.003

Scibiorski, E., Tohver, E., & Jourdan, F. (2015). Rapid cooling and exhumation in the western part of the mesoproterozoic Albany-Fraser Orogen, Western Australia. *Precambrian Research*, *265*, 232–248. https://doi.org/10.1016/j.precamres.2015.02.005

Sengör, A. M. C., Natal'in, B. A., & Burtman, V. S. (1993). Evolution of the Altaid tectonic collage and Palaeozoic crustal growth in Eurasia. *Nature*, *364*(6435), 299–307. https://doi.org/10.1038/364299a0

Shi, Y. R., Jian, P., Kröner, A., Jahn, B. M., Liu, D. Y., Zhang, W., & Ma, H. (2014). Zircon ages and Hf isotopic compositions of plutonic rocks from the Central Tianshan (Xinjiang, northwest China) and their significance for early to mid-Palaeozoic crustal evolution. *International Geology Review*, *56*(11), 1413–1434. https://doi.org/10.1080/00206814.2014.942807

Shi, Y. R., Liu, D. Y., Zhang, Q., Jian, P., Zhang, F. Q., & Miao, L. C. (2007). SHRIMP zircon U-Pb dating of the Gangou granitoids, Central Tianshan Mountains, Northwest China and tectonic significances. *Chinese Science Bulletin*, *52*(11), 1507–1516. https://doi.org/10.1007/s11434-007-0204-2

Shu, L. S., Charvet, J., Guo, L. Z., Lu, H. F., & Laurent-Charvet, S. (1999). A large-scale Palaeozoic dextral ductile strike-slip zone: The Aqqikkudug-Weiya zone along the northern margin of the Central Tianshan belt, Xinjiang, NW China. *Acta Geologica Sinica-English Edition*, *73*(2), 148–162. https://doi.org/10.1111/j.1755-6724.1999.tb00822.x

Shu, L. S., Charvet, J., Lu, H. F., & Laurent, S. C. (2002). Paleozoic accretion-collision events and kinematics of ductile deformation in the eastern part of the Southern-Central Tianshan Belt, China. *Acta Geologica Sinica - English Edition*, *76*(3), 308–323. https://doi.org/10.1111/j.1755-6724.2002.tb00547.x

Shu, L. S., Charvet, J., Lu, H. F., & Laurent, S. C. (2010). Paleozoic accretion-collision events and kinematics of ductile deformation in the eastern part of the Southern-Central Tianshan belt, China. *Acta Geologica Sinica-English Edition*, *76*(3), 308–323. https://doi.org/10.1111/j.1755-6724.2002.tb00547.x

Shu, L. S., Deng, X. L., Zhu, W. B., Ma, D. S., & Xiao, W. J. (2011). Precambrian tectonic evolution of the Tarim Block, NW China: New geochron-ological insights from the Quruqtagh domain. *Journal of Asian Earth Sciences*, *42*(5), 774–790. https://doi.org/10.1016/j.jseaes.2010.08.018

Shu, L. S., Yu, J. H., Charvet, J., Laurent-Charvet, S., Sang, H. Q., & Zhang, R. G. (2004). Geological, geochronological and geochemical features of granulites in the Eastern Tianshan, NW China. *Journal of Asian Earth Sciences*, *24*(1), 25–41. https://doi.org/10.1016/j.jseaes.2003.07.002

Sisson, V. B., Pavlis, T. L., Roeske, S. M., Thorkelson, D. J., Sisson, V. B., Roeske, S. M., et al. (2003). Introduction: An overview of ridge-trench interactions in modern and ancient settings. In *Geology of a transpressional orogen developed during ridge-trench interaction along the North Pacific margin* (Vol. 371). Geological Society of America.

Slama, J., Kosler, J., Condon, D. J., Crowley, J. L., Gerdes, A., Hanchar, J. M., et al. (2008). Plesovice zircon - A new natural reference material for U-Pb and Hf isotopic microanalysis. *Chemical Geology*, *249*(1–2), 1–35. https://doi.org/10.1016/j.chemgeo.2007.11.005

Soldner, J., Štípská, P., Schulmann, K., Yuan, C., Anczkiewicz, R., Jiang, Y. D., et al. (2022a). P–T–t–D records of Early Palaeozoic Andean-type shortening of a hot active margin: The Dunhuang block in NW China. *Journal of Metamorphic Geology*, *41*(1), 59–96. https://doi.org/10.1111/jmg.12688

Soldner, J., Yuan, C., Schulmann, K., Jiang, Y. D., Štípská, P., Zhang, Y. Y., et al. (2022b). Early Paleozoic Cascadia-type active-margin evolution of the Dunhuang block (NW China): Geochemical and geochronological constraints. *GSA Bulletin*, *134*(9–10), 2503–2530. https://doi.org/10.1130/b36220.1

Stampfli, G. M., & Borel, G. D. (2002). A plate tectonic model for the Paleozoic and Mesozoic constrained by dynamic plate boundaries and restored synthetic oceanic isochrons. *Earth and Planetary Science Letters*, *196*(1–2), 17–33. https://doi.org/10.1016/s0012-821x(01)00588-x

Stearns, D. W., & Friedman, M. (1972). Stratigraphic oil and gas fields—Classification, exploration methods, and case histories. In *Stratigraphic oil and gas fields—classification, exploration methods, and case histories*. American Association of Petroleum Geologists and Society of Exploration Geophysicists.

Tagiri, M., Yano, T., Bakirov, A., Nakajima, T., & Uchiumi, S. (1995). Mineral parageneses and metamorphic P-T paths of ultrahigh-pressure eclogites from Kyrghyzstan Tien-Shan. *Island Arc*, *4*(4), 280–292. https://doi.org/10.1111/j.1440-1738.1995.tb00150.x

Tang, G. J., Cawood, P. A., Wyman, D. A., Dan, W., Wang, Q., & Yang, Y. N. (2021). The missing magmatic arc in a long-lived ocean from the Western Kunlun- Pamir Paleo-Tethys Realm. *Geophysical Research Letters*, *48*(22). https://doi.org/10.1029/2021gl095192

Thompson, A. B., Schulmann, K., Jezek, J., & Tolar, V. (2001). Thermally softened continental extensional zones (arcs and rifts) as precursors to thickened orogenic belts. *Tectonophysics*, *332*(1–2), 115–141. https://doi.org/10.1016/s0040-1951(00)00252-3

Tomascak, P. B., Krogstad, E. J., & Walker, R. J. (1996). U-Pb monazite geochronology of granitic rocks from Maine: Implications for late Paleozoic tectonics in the northern Appalachians. *The Journal of Geology*, *104*(2), 185–195. https://doi.org/10.1086/629813

Wan, B., Wang, X. S., Liu, X. J., Cai, K. D., Xiao, W. J., & Mitchell, R. N. (2020). Long-lived seamount subduction in ancient orogens: Evidence from the Paleozoic South Tianshan. *Geology*, *49*(5), 531–535. https://doi.org/10.1130/g48547.1

Wang, B., Chen, Y., Zhan, S., Shu, L. S., Faure, M., Cluzel, D., et al. (2007a). Primary Carboniferous and Permian paleomagnetic results from the Yili Block (NW China) and their implications on the geodynamic evolution of Chinese Tianshan Belt. *Earth and Planetary Science Letters*, *263*(3–4), 288–308. https://doi.org/10.1016/j.epsl.2007.08.037

Wang, B., Faure, M., Cluzel, D., Shu, L. S., Charvet, J., Meffre, S., & Ma, Q. (2006). Late Paleozoic tectonic evolution of the northern West Chinese Tianshan Belt. *Geodinamica Acta*, *19*(3–4), 237–247. https://doi.org/10.3166/ga.19.237-247

Wang, B., Faure, M., Shu, L. S., Cluzel, D., Charvet, J., De Jong, K., & Chen, Y. (2008). Paleozoic tectonic evolution of the Yili Block, western Chinese Tianshan. *Bulletin de la Societe Geologique de France*, *179*(5), 483–490. https://doi.org/10.2113/gssgfbull.179.5.483

Wang, B., Faure, M., Shu, L. S., de Jong, K., Charvet, J., Cluzel, D., et al. (2010). Structural and geochronological study of high-pressure metamorphic rocks in the Kekesu section (northwestern China): Implications for the late paleozoic tectonics of the southern Tianshan. *The Journal of Geology*, *118*(1), 59–77. https://doi.org/10.1086/648531

Wang, B., Liu, H. S., Shu, L. S., Jahn, B. M., Chung, S. L., Zhai, Y. Z., & Liu, D. (2014a). Early Neoproterozoic crustal evolution in northern Yili Block: Insights from migmatite, orthogneiss and leucogranite of the Wenquan metamorphic complex in the NW Chinese Tianshan. *Precambrian Research*, *242*, 58–81. https://doi.org/10.1016/j.precamres.2013.12.006

Wang, B., Shu, L. S., Faure, M., Jahn, B. M., Cluzel, D., Charvet, J., et al. (2011). Paleozoic tectonics of the southern Chinese Tianshan: Insights from structural, chronological and geochemical studies of the Heiyingshan ophiolitic mélange (NW China). *Tectonophysics*, *497*(1–4), 85–104. https://doi.org/10.1016/j.tecto.2010.11.004

Wang, B., Zhai, Y. Z., Kapp, P., de Jong, K., Zhong, L. L., Liu, H. S., et al. (2018). Accretionary tectonics of back-arc oceanic basins in the South Tianshan: Insights from structural, geochronological, and geochemical studies of the Wuwamen ophiolite mélange. *GSA Bulletin*, *130*(1–2), 284–306. https://doi.org/10.1130/b31397.1

Wang, H. Y. C., Chen, H. X., Zhang, Q. W. L., Shi, M. Y., Yan, Q. R., Hou, Q. L., et al. (2017a). Tectonic mélange records the silurian–Devonian subduction-metamorphic process of the southern Dunhuang terrane, southernmost central asian orogenic belt. *Geology*, *45*(5), 427–430. https://doi.org/10.1130/g38834.1

Wang, H. Y. C., Wang, J., Wang, G. D., Lu, J. S., Chen, H. X., Peng, T., et al. (2017b). Metamorphic evolution and geochronology of the Dunhuang orogenic belt in the Hongliuxia area, northwestern China. *Journal of Asian Earth Sciences*, *135*, 51–69. https://doi.org/10.1016/j.jseaes.2016.12.014

Wang, M., Zhang, J. J., Zhang, B., Liu, K., & Ge, M. H. (2016a). Bi-directional subduction of the South Tianshan Ocean during the Late Silurian: Magmatic records from both the southern Central Tianshan Block and northern Tarim craton. *Journal of Asian Earth Sciences*, *128*, 64–78. https://doi.org/10.1016/j.jseaes.2016.07.007

Wang, S., Jiang, Y. D., Weinberg, R., Schulmann, K., Zhang, J., Li, P. F., et al. (2021). Flow of Devonian anatectic crust in the accretionary Altai Orogenic Belt, central Asia: Insights into horizontal and vertical magma transfer. *Geological Society of America Bulletin*, *133*(11–12), 2501–2523. https://doi.org/10.1130/B35645.1

Wang, S. S. (1983). Age determinations of Ar^{40}-K^{40}, Ar^{40}-Ar^{39} and radiogenic ^{40}Ar released characteristics on K-Ar geostandards of China. *Scientia Geologica Sinica*, *4*, 315–323.

Wang, X. S., Gao, J., Klemd, R., Jiang, T., Li, J. L., Zhang, X., et al. (2014b). Geochemistry and geochronology of the Precambrian high-grade metamorphic complex in the Southern Central Tianshan ophiolitic mélange, NW China. *Precambrian Research*, *254*, 129–148. https://doi.org/10.1016/j.precamres.2014.08.017

Wang, X. S., Gao, J., Klemd, R., Jiang, T., Li, J. L., Zhang, X., & Xue, S. C. (2017). The Central Tianshan Block: A microcontinent with a Neoarchean-Paleoproterozoic basement in the southwestern Central Asian Orogenic Belt. *Precambrian Research*, *295*, 130–150. https://doi.org/10.1016/j.precamres.2017.03.030

Wang, X. S., Klemd, R., Gao, J., Jiang, T., & Zhang, X. (2020). Early Devonian tectonic conversion from contraction to extension in the Chinese Western Tianshan: A response to slab rollback. *GSA Bulletin*, *133*(7–8), 1613–1633. https://doi.org/10.1130/b35760.1

Wang, X. S., Klemd, R., Li, J. L., Gao, J., Jiang, T., Zong, K. Q., & Xue, S. (2022). Paleozoic subduction-accretion in the Southern Central Asian Orogenic Belt: Insights from the Wuwamen accretionary complex of the Chinese South Tianshan. *Tectonics*, *41*(2). https://doi.org/10.1029/2021tc006965

Wang, Z. H., Qi, Y. P., & Bergström, S. M. (2007). Ordovician conodonts of the Tarim Region, Xinjiang, China: Occurrence and use as paleoenvironment indicators. *Journal of Asian Earth Sciences*, *29*(5–6), 832–843. https://doi.org/10.1016/j.jseaes.2006.05.007

Wang, Z. H., Sun, S., Li, J. L., Hou, Q. L., Qin, K. Z., Xiao, W. J., & Hao, J. (2003). Paleozoic tectonic evolution of the northern Xinjiang, China: Geochemical and geochronological constraints from the ophiolites. *Tectonics*, *22*(2). https://doi.org/10.1029/2002tc001396

Wang, Z. W., Pei, F. P., Xu, W. L., Cao, H. H., Wang, Z. J., & Zhang, Y. (2016b). Tectonic evolution of the eastern Central Asian Orogenic Belt: Evidence from zircon U–Pb–Hf isotopes and geochemistry of early Paleozoic rocks in Yanbian region, NE China. *Gondwana Research*, *38*, 334–350. https://doi.org/10.1016/j.gr.2016.01.004

Weinberg, R. F., Hasalova, P., Ward, L., & Fanning, C. M. (2013). Interaction between deformation and magma extraction in migmatites: Examples from Kangaroo Island, South Australia. *Geological Society of America Bulletin*, *125*(7–8), 1282–1300. https://doi.org/10.1130/b30781.1

White, A. J. R., & Chappell, B. W. (1988). Some supracrustal (S-type) granites of the Lachlan fold belt. *Earth and Environmental Science Transactions of the Royal Society of Edinburgh*, *79*(2–3), 169–181. https://doi.org/10.1017/S026359330001419X

Wiedenbeck, M., AllÉ, P., Corfu, F., Griffin, W. L., Meier, M., Oberli, F., et al. (1995). Three natural zircon standards for U-Th-Pb, Lu-Hf, trace element and Ree analyses. *Geostandards and Geoanalytical Research*, *19*(1), 1–23. https://doi.org/10.1111/j.1751-908X.1995.tb00147.x

Wilhem, C., Windley, B. F., & Stampfli, G. M. (2012). The Altaids of Central Asia: A tectonic and evolutionary innovative review. *Earth-Science Reviews*, *113*(3–4), 303–341. https://doi.org/10.1016/j.earscirev.2012.04.001

Wilson, M. (1993). Magmatism and the geodynamics of basin formation. *Sedimentary Geology*, *86*(1–2), 5–29. https://doi.org/10.1016/0037-0738(93)90131-n

Windley, B. F., Alexeiev, D., Xiao, W. J., Kroner, A., & Badarch, G. (2007). Tectonic models for accretion of the Central Asian Orogenic Belt. *Journal of the Geological Society*, *164*(1), 31–47. https://doi.org/10.1144/0016-76492006-022

Windley, B. F., Allen, M. B., Zhang, C., Zhao, Z. Y., & Wang, G. R. (1990). Paleozoic accretion and Cenozoic redeformation of the Chinese Tien Shan Range, central Asia. *Geology*, *18*(2), 128. https://doi.org/10.1130/0091-7613(1990)018

Wu, H. X., Dilek, Y., Zhang, F. Q., Chen, H. L., Chen, H., Wang, C. Y., et al. (2022a). Ediacaran magmatism and rifting along the northern margin of the Tarim craton: Implications for the late Neoproterozoic Rodinia configuration and breakup. *GSA Bulletin*, *135*(1–2), 367–388. https://doi.org/10.1130/b36305.1

Wu, H. X., Zhang, F. Q., Dilek, Y., Chen, H. L., Wang, C. Y., Lin, X. B., et al. (2022b). Mid–Neoproterozoic collision of the Tarim Craton with the Yili–Central Tianshan Block towards the final assembly of supercontinent Rodinia: A new model. *Earth-Science Reviews*, *228*, 103989. https://doi.org/10.1016/j.earscirev.2022.103989

Xiao, W. J., Han, C. M., Yuan, C., Chen, H. L., Li, Z. L., Sun, M., et al. (2005). Paleozoic reconstruction and tectonic evolution of North Xinjiang, NW China: Implications for the lateral growth of Central Asia. *Mineral Deposit Research: Meeting the Global Challenge*, *1*, 1355–1358. https://doi.org/10.1007/3-540-27946-6_345

Xiao, W. J., Han, C. M., Yuan, C., Sun, M., Lin, S. F., Chen, H. L., et al. (2008). Middle Cambrian to Permian subduction-related accretionary orogenesis of Northern Xinjiang, NW China: Implications for the tectonic evolution of central Asia. *Journal of Asian Earth Sciences*, *32*(2–4), 102–117. https://doi.org/10.1016/j.jseaes.2007.10.008

Xiao, W. J., Song, D. F., Windley, B. F., Li, J. L., Han, C. M., Wan, B., et al. (2020). Accretionary processes and metallogenesis of the Central Asian Orogenic Belt: Advances and perspectives. *Science China Earth Sciences*, *63*(3), 329–361. https://doi.org/10.1007/s11430-019-9524-6

Xiao, W. J., Windley, B. F., Allen, M. B., & Han, C. M. (2013). Paleozoic multiple accretionary and collisional tectonics of the Chinese Tianshan orogenic collage. *Gondwana Research*, *23*(4), 1316–1341. https://doi.org/10.1016/j.gr.2012.01.012

Xiao, W. J., Windley, B. F., Huang, B. C., Han, C. M., Yuan, C., Chen, H. L., et al. (2009a). End-Permian to mid-Triassic termination of the accretionary processes of the southern Altaids: Implications for the geodynamic evolution, Phanerozoic continental growth, and metallogeny of Central Asia. *International Journal of Earth Sciences*, *98*(6), 1189–1217. https://doi.org/10.1007/s00531-008-0407-z

Xiao, W. J., Windley, B. F., Sun, S., Li, J. L., Huang, B. C., Han, C. M., et al. (2015). A Tale of amalgamation of three permo-Triassic collage systems in Central Asia: Oroclines, sutures, and terminal accretion. *Annual Review of Earth and Planetary Sciences*, *43*(1), 477–507. https://doi.org/10.1146/annurev-earth-060614-105254

Xiao, W. J., Windley, B. F., Yong, Y., Yan, Z., Yuan, C., Liu, C. Z., & Li, J. (2009b). Early Paleozoic to Devonian multiple-accretionary model for the Qilian Shan, NW China. *Journal of Asian Earth Sciences*, *35*(3–4), 323–333. https://doi.org/10.1016/j.jseaes.2008.10.001

Xu, B., Charvet, J., Chen, Y., Zhao, P., & Shi, G. Z. (2013). Middle Paleozoic convergent orogenic belts in western Inner Mongolia (China): Framework, kinematics, geochronology and implications for tectonic evolution of the Central Asian Orogenic Belt. *Gondwana Research*, *23*(4), 1342–1364. https://doi.org/10.1016/j.gr.2012.05.015

Xu, B., Jian, P., Zheng, H. F., Zou, H. B., Zhang, L. F., & Liu, D. Y. (2005). U–Pb zircon geochronology and geochemistry of Neoproterozoic volcanic rocks in the Tarim Block of northwest China: Implications for the breakup of Rodinia supercontinent and Neoproterozoic glaciations. *Precambrian Research*, *136*(2), 107–123. https://doi.org/10.1016/j.precamres.2004.09.007

Xu, B., Zou, H. B., Chen, Y., He, J. Y., & Wang, Y. (2013). The Sugetbrak basalts from northwestern Tarim Block of northwest China: Geochronology, geochemistry and implications for Rodinia breakup and ice age in the Late Neoproterozoic. *Precambrian Research*, *236*, 214–226. https://doi.org/10.1016/j.precamres.2013.07.009

Xu, Z. Q., Li, S. T., Zhang, J. X., Yang, J. S., He, B. Z., Li, H. B., et al. (2011). Paleo-Asian and Tethyan tectonic systems with docking the Tarim block. *Acta Petrologica Sinica*, *27*(1), 1–22.

Yang, H., Zhang, H. F., Luo, B. J., Zhang, J., Xiong, Z. L., Guo, L., & Pan, F. (2015). Early Paleozoic intrusive rocks from the eastern Qilian orogen, NE Tibetan Plateau: Petrogenesis and tectonic significance. *Lithos*, *224–225*, 13–31. https://doi.org/10.1016/j.lithos.2015.02.020

Yang, S., Ge, R. F., Zhou, T., & Wang, Y. (2022). Decoupling of metamorphic zircon U-Pb ages and P-T paths in the Dunhuang metamorphic complex, northwestern China. *Precambrian Research*, *379*, 106783. https://doi.org/10.1016/j.precamres.2022.106783

Yang, S. H., & Zhou, M. F. (2009). Geochemistry of the ~430-Ma Jingbulake mafic–ultramafic intrusion in Western Xinjiang, NW China: Implications for subduction related magmatism in the South Tianshan orogenic belt. *Lithos*, *113*(1–2), 259–273. https://doi.org/10.1016/j.lithos.2009.07.005

Zhang, C., Li, X., Li, Z., Lu, S., Ye, H., & Li, H. (2007). Neoproterozoic ultramafic–mafic-carbonatite complex and granitoids in Quruqtagh of northeastern Tarim Block, western China: Geochronology, geochemistry and tectonic implications. *Precambrian Research*, *152*(3–4), 149–169. https://doi.org/10.1016/j.precamres.2006.11.003

Zhang, C. L., Li, H. K., Santosh, M., Li, Z. X., Zou, H. B., Wang, H. Y., et al. (2012a). Precambrian evolution and cratonization of the Tarim Block, NW China: Petrology, geochemistry, Nd-isotopes and U–Pb zircon geochronology from Archaean gabbro-TTG–potassic granite suite and Paleoproterozoic metamorphic belt. *Journal of Asian Earth Sciences*, *47*, 5–20. https://doi.org/10.1016/j.jseaes.2011.05.018

Zhang, C. L., Zou, H. B., Li, H. K., & Wang, H. Y. (2013). Tectonic framework and evolution of the Tarim Block in NW China. *Gondwana Research*, *23*(4), 1306–1315. https://doi.org/10.1016/j.gr.2012.05.009

Zhang, C. L., Zou, H. B., Wang, H. Y., Li, H. K., & Ye, H. M. (2012b). Multiple phases of the Neoproterozoic igneous activity in Quruqtagh of the northeastern Tarim Block, NW China: Interaction between plate subduction and mantle plume? *Precambrian Research*, *222–223*, 488–502. https://doi.org/10.1016/j.precamres.2011.08.005

Zhang, L., Zhang, J. F., & Jin, Z. M. (2016). Metamorphic P–T–water conditions of the Yushugou granulites from the southeastern Tianshan orogen: Implications for Paleozoic accretionary orogeny. *Gondwana Research*, *29*(1), 264–277. https://doi.org/10.1016/j.gr.2014.12.009

Zhang, L. F., Ellis, D. J., & Jiang, W. B. (2002). Ultrahigh-pressure metamorphism in western Tianshan, China: Part I. Evidence from inclusions of coesite pseudomorphs in garnet and from quartz exsolution lamellae in omphacite in eclogites. *American Mineralogist*, *87*(7), 853–860. https://doi.org/10.2138/am-2002-0707

Zhang, S. H., Zhao, Y., Ye, H., Liu, J. M., & Hu, Z. C. (2014). Origin and evolution of the Bainaimiao arc belt: Implications for crustal growth in the southern Central Asian orogenic belt. *Geological Society of America Bulletin*, *126*(9–10), 1275–1300. https://doi.org/10.1130/b31042.1

Zhang, Z. Y., Zhu, W. B., Zheng, D. W., Zheng, B. H., Xiao, W. J., Li, D. M., & Han, C. (2017). Neoproterozoic-Paleozoic tectonic evolution of the northeastern Tarim block: Constraints from40Ar/39Ar geochronology in the Kuluketage Area, NW China. *Acta Geologica Sinica - English Edition*, *91*(4), 1231–1247. https://doi.org/10.1111/1755-6724.13357

Zhao, G. C., Wang, Y. J., Huang, B. C., Dong, Y. P., Li, S. Z., Zhang, G. W., & Yu, S. (2018). Geological reconstructions of the East Asian blocks: From the breakup of Rodinia to the assembly of Pangea. *Earth-Science Reviews*, *186*, 262–286. https://doi.org/10.1016/j.earscirev.2018.10.003

Zhong, L. L., Wang, B., Alexeiev, D. V., Cao, Y. C., Biske, Y. S., Liu, H. S., et al. (2017). Paleozoic multi-stage accretionary evolution of the SW Chinese Tianshan: New constraints from plutonic complex in the Nalati Range. *Gondwana Research*, *45*, 254–274. https://doi.org/10.1016/j.gr.2016.12.012

Zhong, L. L., Wang, B., de Jong, K., Zhai, Y. Z., & Liu, H. S. (2019). Deformed continental arc sequences in the South Tianshan: New constraints on the Early Paleozoic accretionary tectonics of the Central Asian Orogenic Belt. *Tectonophysics*, *768*, 228169. https://doi.org/10.1016/j.tecto.2019.228169

Zhong, L. L., Wang, B., Shu, L. S., Liu, H. S., Mu, L. X., Ma, Y. Z., & Zhai, Y. (2015). Structural overprints of early Paleozoic arc-related intrusive rocks in the Chinese Central Tianshan: Implications for Paleozoic accretionary tectonics in SW Central Asian Orogenic Belts. *Journal of Asian Earth Sciences*, *113*, 194–217. https://doi.org/10.1016/j.jseaes.2014.12.003

Zhou, D. (2001). *Paleozoic tectonic amalgamation of the Chinese tian Shan: Evidence from a transect along the Dushanzi-Kuqa Highway*. Memoir of the Geological Society of America. https://doi.org/10.1130/0-8137-1194-0.23

Zhou, D., Graham, S. A., Chang, E. Z., Wang, B. Y., & Hacker, B. (2001). *Paleozoic tectonic amalgamation of the Chinese Tian Shan: Evidence from a transect along the Dushanzi-Kuqa Highway* (Vol. 194, pp. 23–46). Geological Society of America Memoirs. https://doi.org/10.1130/0-8137-1194-0.23

Zhou, D. W. (2004). Zircon U-Pb SHRIMP ages of high-pressure granulite in Yushugou ophiolitic terrane in southern Tianshan and their tectonic implications. *Chinese Science Bulletin*, *49*(13), 1415. https://doi.org/10.1360/03wd0598

Zhu, T., Wang, H. L., Zhao, Y., Xu, X. Y., Li, Z. P., & Li, S. (2019a). Palaeozoic diorites from the south-western Dunhuang terrane, NW China: Constraints on tectonic evolution of southernmost CAOB. *Geological Journal*, *55*(1), 893–911. https://doi.org/10.1002/gj.3447

Zhu, W. B., Zhang, Z. Y., Shu, L. S., Lu, H. F., Su, J. B., & Yang, W. (2008). SHRIMP U-Pb zircon geochronology of Neoproterozoic Korla mafic dykes in the northern Tarim Block, NW China: Implications for the long-lasting breakup process of Rodinia. *Journal of the Geological Society*, *165*(5), 887–890. https://doi.org/10.1144/0016-76492007-174

Zhu, W. B., Zheng, B. H., Shu, L. S., Ma, D. S., Wu, H. L., Li, Y. X., et al. (2011). Neoproterozoic tectonic evolution of the Precambrian Aksu blueschist terrane, northwestern Tarim, China: Insights from LA-ICP-MS zircon U–Pb ages and geochemical data. *Precambrian Research*, *185*(3–4), 215–230. https://doi.org/10.1016/j.precamres.2011.01.012

Zhu, X., Wang, B., Chen, Y., & Liu, H. S. (2019b). Constraining the intracontinental tectonics of the SW Central Asian Orogenic Belt by the Early Permian Paleomagnetic Pole for the Turfan-Hami Block. *Journal of Geophysical Research: Solid Earth*, *124*(12), 12366–12387. https://doi.org/10.1029/2019jb017680

Zhu, X., Wang, B., Chen, Y., Liu, H. S., Horng, C. S., Choulet, F., et al. (2018). First Early Permian Paleomagnetic Pole for the Yili Block and its implications for Late Paleozoic postorogenic kinematic evolution of the SW Central Asian Orogenic Belt. *Tectonics*, *37*(6), 1709–1732. https://doi.org/10.1029/2017tc004642

Zhu, Z. X., Li, J. Y., Dong, L. H., Wang, K. Z., Liu, G. Z., Li, Y. P., et al. (2008b). Age determination and geological significance of Devonian granitic intrusions in Seriyakeyilake region, northern margin of Tarim basin, Xinjiang. *Acta Petrologica Sinica*, *24*(5), 971–976.

Erratum

In the originally published version of this article, grant information for the National Science Foundation of China (42372240) was inadvertently omitted. This grant information has now been added to the Acknowledgments section of the article, and this may be considered the authoritative version of record.